Control of brine composition over reactive transport processes in calcium carbonate rock dissolution: Time-lapse imaging of evolving dissolution patterns

Control of brine composition over reactive transport processes in calcium carbonate rock dissolution: time-lapse imaging of evolving dissolution patterns

Priyanka Agrawal*[1], Hamed Aslannejad[1], Arjen Mascini[2], Tom Bultreys[2], Amir Raoof[1], Veerle Cnudde[1,2], Ian B. Butler[3] and Mariëtte Wolthers*[1]

[1]Department of Earth Sciences, Utrecht University, Utrecht, Netherlands,

[2]PProGRess/UGCT, Department of Geology, Ghent University, Ghent, Belgium

[3]School of Geosciences, University of Edinburgh, Edinburgh

*Corresponding Authors: p.agrawal@uu.nl, m.wolthers@uu.nl

Highlights

- Ketton rock was dissolved using solutions with different salinities
- Amount of Ca^{2+} and NaCl salt in solution impacts the dissolution patterns
- Salinity exhibits an opposing influence on dissolution rate and calcite solubility.
- Time-lapse imaging reveals the distinct structural evolution of the dissolution patterns

***Keywords*:** Carbonate dissolution; Micro-CT; Reactive transport; Acid well stimulation; Wormhole formation; Porosity-Permeability relation

Abstract

This study investigates the impact of brine composition—specifically calcium ions and NaCl-based salinity—on the development of dissolution features in Ketton, a porous calcium carbonate rock. Utilizing a laboratory XMT (X-ray microtomography) scanner, we captured time-lapse in situ images of Ketton samples throughout various dissolution experiments, conducting four distinct flow-through experiments with differing brine solutions at a flow rate of 0.26 ml min^{-1}. The scans yielded a voxel size of 6 µm, enabling the assessment of the temporal evolution of porosity and pore structure through image analysis and permeability

evaluations via single-phase fluid flow simulations employing direct numerical solutions and network modeling, as opposed to direct measurement.

Time-lapse imaging technique has delineated the extent to which the concentrations of $CaCl_2$ and NaCl in the injecting solution control the structural evolution of dissolution patterns, subsequently triggering the development of characteristic dissolution pattern. The inflow solution with no Ca^{2+} ions and with the minimal salt content manifested maximum dissolution near the sample inlet, coupled with the formation of numerous dissolution channels, i.e., wormholes. Conversely, solutions with a trace amount of Ca^{2+} ions induced focused dissolution, resulting in the formation of sparsely located channels. Inflow solutions with high concentrations of both Ca^{2+} ions and salt facilitated uniformly dispersed dissolution, primarily within microporous domains, initiating particle detachment and displacement and leading to localized pore-clogging. The relative increase in permeability, in each experiment, was correlated with the developed dissolution pattern. It was discerned that varying ratios of salt and calcium concentrations in the injected solution systematically influenced image-based permeability simulations and porosity, allowing for the depiction of an empirical porosity-permeability relationship.

1. INTRODUCTION

Carbonate formations constitute ~20% of sedimentary basins and ~60% of the world's hydrocarbon reservoirs (Morse and Mackenzie, 1990; Akbar et.al., 2000; Schlumberger 2019) and calcite is the dominant mineral in these reservoirs. Applications such as CO_2 sequestration or acid stimulation for enhanced oil and gas production from carbonate reservoirs involve the interaction of an acidic fluid with the calcite. This leads to the dissolution of calcite and the creation of secondary porosity and permeability.

Numerous studies have shown that parameters such as injection rate, the acidity of the injected solution, and initial heterogeneity of the porous medium can impact the dissolution processes and control the subsequent evolution of rock properties (e.g., Esteves et al., 2020; Golfier et al., 2002; Hoefner and Fogler, 1988; Luquot and Gouze, 2009; Meile and Tuncay, 2006; Menke et al., 2017; Soulaine et al., 2017; Yoo et.al., 2021). In particular, dissolution kinetics along with the acid injection rate is known to form characteristic dissolution pattern (e.g., Daccord et al., 1993; Elkhoury et al., 2013; Golfier et al., 2002; Hoefner et al., 1987; Hoefner and Fogler, 1988; Luquot et al., 2014; Luquot and Gouze, 2009; Maheshwari et al., 2013; Panga et al., 2005). At the pore scale, the interaction of an acid with calcite mineral is a combination of two processes: (i) the transport rate of the aqueous ions to and from the mineral surface and (ii) the dissolution reaction taking place at the mineral surface. Manipulation of the rate of any of these processes affects the effective dissolution rate and consequently the dissolution patterns. In general, five types of dissolution patterns have been reported, corresponding to different dissolution kinetics for a given acid injection rate (e.g., Fredd and Fogler 1998; Hoefner and Fogler, 1988; Maheshwari et.al., 2013; Soulaine et al., 2017): 1) face dissolution, 2) conical wormholes, 3) dominant wormholes, 4) ramified wormholes, and (5) uniform dissolution. For example, when the injected solution is highly reactive such that the transport time scale of the acid is longer compared to the reaction time scale of the acid, the acid is mostly consumed to dissolve the rock close to its inlet face. This leads to the development of the face dissolution pattern. Acid solutions with low reactivity, on the other hand, can penetrate further into the rock, causing uniform dissolution since time scale of transport becomes smaller than the time scale of chemical reaction. In summary, with decrease in the dissolution rate, the dissolution regime changes from the face dissolution regime to the uniform dissolution regime, while passing through the intermediate regimes corresponding to the different wormhole dissolution patterns. These patterns have a major

control on the required amount of acid volume that needs to flow through the sample to achieve specific permeability increase for the same amount of porosity increment (e.g., Fredd and Fogler 1998; Hoefner and Fogler, 1988; Maheshwari et.al., 2013; Soulaine et. al., 2017; Yoo et.al., 2021). For example, among the five dissolution patterns, the dominant wormholes are the most conducting channels and require the least volume of acid injection to enhance the permeability by a certain amount.

One way of controlling which dissolution regime is achieved in reactive-transport dissolution is by addition of dissolution-inhibiting or -enhancing compounds. Examples are the addition of microemulsion (Hoefner et al., 1987), varying the CO_2 concentration (Luquot et al., 2014) or using SO_4^{2-} ions in the injected acid (Garcia-Rios et al., 2015). Luquot et al., 2014 showed that high pCO_2 developed preferential flow paths while lower pCO_2 resulted in uniform dissolution. Garcia-Rios et al., 2015 observed the inhibitory effect of SO_4^{2-} ions on calcite dissolution rates while observing no significant effect on the created dissolution patterns.

The impact of salinity and dissolution-inhibiting or -enhancing ions and compounds present in formation water on pore geometry evolution during dissolution of porous carbonate rocks is less well-known. Hanor (1994) reported that the salinities of pore waters in subsurface basins may span over five orders of magnitude i.e., from few mg l^{-1} in shallow meteoric systems to over 400000 mg l^{-1} in evaporite-rich sedimentary basin such as Michigan Basin, in USA. Moreover, in the formation brines, Ca^{2+} is the second most abundant cation after Na^{+}. The concentration of Ca^{2+} can even exceed the Na^{+} concentration in formation waters with salinities higher than 300000 mg l^{-1} (Gledhill and Morse, 2006). Therefore, understanding the geochemistry of high salinity and Ca^{2+} rich formation waters is important in the assessment of (the permeability evolution in) carbonate minerals enriched sedimentary basins for applications such as CO_2 sequestration or acid stimulation for enhanced oil production.

Several batch dissolution experiments have examined the influence of the salinity of the solution and Ca^{2+} concentration on the calcite dissolution rates (Anabaraonye et al., 2019; Buhmann and Dreybrodt, 1987; Finneran and Morse, 2009; Gledhill and Morse, 2006; Gutjahr et al., 1996; Pokrovsky et al., 2005; Sjöberg and Rickard, 1985). For transport-controlled dissolution regime, no impact of the NaCl-based ionic strength on calcite dissolution rates is observed when I <1M (Pokrovsky et.al., 2005), while strong inhibition of calcite dissolution rates is observed with NaCl-salinity >1M (Gledhill and Morse, 2006). The impact of Ca^{2+} ions in solution on the dissolution rate is contested in literature. Some authors found that calcium inhibits calcite dissolution in neutral to basic conditions only (Sjoberg and Rickard,1985), while others found that calcium ions enhance calcite dissolutions rates (Gutjahr et al. 1996; Gledhill and Morse 2006).

While there is a clear, albeit incoherent, impact of calcium and salinity on calcium carbonate dissolution rates, the implication of this influence on the development of secondary porosity and permeability in carbonate rocks is unknown. We are not aware of any reactive flow experimental studies that have explored the control of NaCl and Ca^{2+} concentration on the dissolution patterns.

Through time-lapse imaging, we have examined the influence of the amount of NaCl and Ca^{2+} ions in the injected solution over the structural evolution of dissolution patterns and subsequent development of characteristic dissolution pattern in Ketton samples. We present the results of four flow experiments using different acidic solutions with constant flow rate into four samples of oolitic limestone. The composition of these solutions, i.e., amount of salt and Ca^{2+} ions, was chosen to cover a wide range of dissolution kinetics. X-ray microtomography (XMT) image analysis and effluent analysis were used to calculate the removed mass of calcite and consequent changes in the porosity of the samples. The link between dissolution and permeability enhancement of the samples was investigated using

numerical simulation of single-phase flow using two approaches: pore network modelling (PNM) approach utilizing the pore network extracted from the XMT images and direct numerical simulation (DNS) method, also utilizing the XMT images. Finally, for each experiment, development in permeability was related to the modified porosity of the sample.

2. MATERIAL AND METHODS

For this study, we have utilized a relatively homogeneous carbonate rock type: Ketton limestone. This oolitic limestone is a part of the Lincolnshire Formation, which was deposited around 165 million years ago. Four cylindrical shape samples named K1, K2, K3, and K4, of 6 mm in diameter and ~12mm in length were drilled side by side out of a limestone block. Calcite-equilibrated solutions were prepared using deionized water at an atmospheric pressure and room temperature conditions. The composition of these solutions calculated using PHREEQC (Parkhurst and Appelo, 2013) and Pitzer database is provided in Table S1. The samples were pre-saturated using a protocol based on that of Boone et al. (2014) outside of the flow cell under vacuum condition with a calcite-equilibrated solution for about 48hrs. After mounting the pre-saturated sample in the flow cell, any air still present in the sample was flushed by flowing the calcite-equilibrated solution through the sample for ~2000 pore volumes at three flow rates, 10 ml min^{-1}, 5 ml min^{-1} and 1 ml min^{-1}. Then an image was taken to visually verify that no air was present within the sample and the full saturation of the pore space was achieved. To impose a uniform radial fluid at the injection face of the sample, an inert porous sintered glass plug (Robu glass por 0 filter) was placed in front of the inlet side of the carbonate plug. Both plugs were inserted into a Viton sleeve, placed in a custom-built Hassler-type flow cell made from X-ray transparent PEEK. A confining pressure of ~20 bar was applied on the sleeve to avoid fluid bypassing the sample. The fit of the sleeve to the sample was assessed visually on the raw data and was observed to

fit very tightly (Figure S1). Additionally, the confinement pressure meter indicated a consistent pressure of ~20 bar during the experiment, indicating a leak-free flow.

Note that flow was established from bottom to top of the sample while all presented images in the subsequent sections are upside down. All experiments were performed under room temperature and a confining pressure of ~20 bars.

2.1 Chemical composition of injecting solutions

Four solutions with the same HCl concentration of 0.001 mol dm^{-3} but different salinity and Ca^{2+} concentration was prepared. All solutions were prepared by adding the appropriate amount of the reagents with, $CaCl_2$, NaCl, and HCl to deionized water under atmospheric conditions. pH values of these solutions are provided in Table 1. The first solution had an ionic strength of 0.2 mol dm^{-3}, without calcium ions (referred to as no calcium low salinity solution, or NCLS). A second solution had a similar ionic strength but contained 1×10^{-3} mol dm^{-3} of Ca^{2+} ions (low calcium low salinity solution, or LCLS). The third type of solution had an ionic strength of 1.2 mol dm^{-3}, without calcium ions (no calcium high salinity solution, or NCHS). Finally, the fourth solution had a similar ionic strength as the third but contained 0.335 mol dm^{-3} of Ca^{2+} ions (high calcium high salinity solution, or HCHS). For all four experiments, acidic solutions were injected with a same and constant flow rate of 4.16×10^{-9} m^3s^{-1} (i.e., Q = 0.26 ml min^{-1}).

The concentration of Ca^{2+} ions in inflow and outflow solutions was measured with the ICP-OES method. This method can measure Ca^{2+} concentration within a range of $0.5\text{-}5 \times 10^{-3}$ mol dm^{-3}. Therefore, most of the solutions were diluted using 0.7M HNO_3 acid, to a dilution ratio of 1:100, while some of the solutions related to experiment HCHS were diluted by a ratio of 1:1000. The pH of the original inflow and outflow solutions (i.e., without

dilution) was measured with a pH 3110 portable pH meter and pH electrode SenTix™ or (for the HCHS experiment) WTW - Sensolyt 900-P.

The solution composition of all inflow solutions was calculated using PHREEQC (Parkhurst and Appelo, 2013) with the Pitzer database. These calculations showed that the activity coefficient of H^+ is close to unity for all solutions (Table S1). For inflow solutions NCLS and LCLS, the measured value of pH matched with the calculated value of pH. It should be noted that the measured pH values for the NCHS and the HCHS was affected by the non-compatibility of the utilized electrode with the high concentration of ions in the solutions. As a consequence, the measured value of pH of these solutions using above mentioned electrode differed from the calculated value of pH. In order to clarify the uncertainties over pH values, we have re-measured pH with a different pH electrode WTW - Sensolyt 900-P and multimeter WTW portable pH meter Multiline Multi 3630 IDS. These measurements were performed on a separate solution prepared with the same recipe as that of the inflow solution for experiment HCHS. A measured pH value of 3.03 for this solution using pH electrode WTW - Sensolyt 900-P further affirms the non-compatibility of the pH electrode SenTix™ for measurements in high salt (calcium and chloride) solutions. Table 1 summarizes experimental details related to flow and solution chemistry. Note that the Pitzer model is not tailored to the exact conditions at the start of, and during our experiments. Therefore, the SI's calculated for calcite (Table 1) should be treated with caution.

2.2 Data acquisition and processing

In situ imaging of the sample was performed using a laboratory-based environmental micro-CT scanner built at Ghent University (Bultreys et al., 2016). The starting step of each experiment was the saturation of the sample with calcite-equilibrated water, followed by scanning of the sample. The scanning was performed with an X-ray beam energy of 110kV and an exposure time of 80ms. The reconstructed voxel size of the images was 6 μm per

voxel and three stacks were required to cover the full length of the sample. Such full sample length scanning was performed at the beginning and the end of the experiment. During acid injection, the scanner was fixed near the inlet of the sample; therefore, time-lapse scans correspond to the top ~6 mm section of the sample. Hereafter, these time-lapse scans are referred as half-length sample volumes. For both full-length scans and half-length scans, a total of 2200 projections, covering a 360° rotation of the scanner, were obtained in 15 minutes. Details on the processing steps of both types of scans is provided in SI Section 1.

2.3 Skeleton analysis

In this study, we used the skeletonization methods to characterize the wormholes created during limestone dissolution. The skeletonization workflow converts the three-dimensional pore space into a one-dimensional object while preserving topological and geometrical features. This process of dimension reduction includes iterative removal of individual voxels from a volume until a single line of voxels (i.e., the medial axis of the volume) remains along the pore space. This yields a simplified skeleton representation of the pore space, in which each voxel stores properties of the original complex 3D pore space through attributes like thickness, orientation and length. Detailed steps on the skeletonization of wormholes and subsequent quantification of the wormhole are provided in SI Sections S2 and S3, respectively.

2.4 Pore network extraction and flow modelling

We have calculated the velocity field and permeability of the sample at a different stage of the dissolution process. For this purpose, we have utilized a pore network model because it requires less computational time than direct numerical simulation. Single phase flow was simulated on the extracted pore network. For simulating flow, the inlet face of the network was maintained at a constant value of Darcy velocity (i.e., constant average pore inlet

velocity) and the outlet face at an atmospheric pressure condition, after which the pressure and velocity in each pore were found by imposing mass conservation. The Darcy velocity was calculated as:

$$u_D = \frac{Q}{A} \quad (1)$$

where, Q is the volumetric flow rate (m^3 s^{-1}) and A is the cross-section area of the sample (m^2).

From the Darcy velocity (u_D) and pressure difference between the inlet and outlet faces (ΔP_{PNM}), the permeability of the network is obtained from:

$$k_{PNM} = \frac{\mu\, u_D\, L}{\Delta P_{PNM}} \quad (2)$$

where, μ is the viscosity of water, 0.001 Pa.s, and L is the pore network length along the flow direction.

The remaining boundaries of the network parallel to the flow direction were implemented as no-flow boundaries. Further details on the modeled equations can be found in Raoof et al. (2012).

2.5 Direct flow simulation of pore-scale images

In order to evaluate the permeability changes during dissolution, XMT images which were acquired at the start and end of the experiment were used as 3D pore space domains for the microscale fluid flow simulation.

The XMT-based pore spaces were first simplified and scaled using open-source image processing software, MeshLab (MeshLab, version 2021.05; https://www.meshlab.net). The resulting pore space was used for fluid flow simulations under same flow direction as that of

experiments. Flow equation were solved with a pressure difference imposed on either side of the sample and a no-slip boundary condition at the lateral faces of the domain.

OpenFOAM, an open-source CFD toolbox, was used to perform single phase flow simulation (Aslannejad et al., 2018; Bedram and Moosavi, 2011). For meshing purposes, a native meshing tool of OpenFOAM (in this case, snappyHexMesh) was used. The flow simulation required a significant number of discretization cells (i.e., base refinement level: 100 × 100 × 250); therefore, the parallel computation was done using 8-cores. Classic Semi-Implicit Method for Pressure Linked Equations (SIMPLE) algorithm was used to solve flow equation.

Absolute permeability, k_{DNS} (m^2) was calculated using the Darcy equation:

$$k_{DNS} = \frac{\mu\, Q\, L_x}{\Delta P_{DNS}\, L_y\, L_z} \tag{3}$$

where, Q ($m^3.s^{-1}$) is flow rate, L_x, L_y and L_z are the domain dimensions in each direction and ΔP_{DNS} is the imposed pressure difference. A mesh sensitivity study was performed by varying the number of discretization cells in the x, y, and z directions. Along with the base refinement level, two more refinement levels i.e., refinement level 1: 100 × 100 × 150 and refinement level 2: 200 × 200 × 250, were simulated. Cropped sample length-based dataset of Sample K1 belonging to the start and end of the experiment was utilized. We observed that a 4x increment in discretization cell numbers (base refinement level and refinement level 2) results in ~8% permeability variation for the unreacted rock volume and ~18% permeability variation for the dissolved rock volume, while the relative change in permeability due to dissolution is comparable among different mesh configurations (Figure S2).

2.6 Sample characterization prior to experiments

Characterization of the Ketton samples is based on the XMT images, FIB-SEM images, EDS analysis, XRD analysis, and properties of the extracted pore networks.

XMT images showed that Ketton is composed of spherical grains and can be considered a relatively homogeneous carbonate rock at the macroscopic scale (Figure S1 and S4). Electron microscopy imaging of the surface and cross-sectional view of a randomly chosen spherical grain were done using FIB-SEM imaging technique. Results showed the extent of the intra-grain porosity (Figure S7). SEM images of the part of the sample showed textural heterogeneity at a microscopic scale (Figure S8). We observed that some part of the grain was made of rhombohedral particles, which is a typical morphology of calcite. Other parts of the grain were made of needle-shaped particles, which is a typical morphology of aragonite (e.g. Nan et al., 2008). EDS analysis suggested that these particles were majorly composed of Ca, C and O (Figure S9).

In order to identify the particle polymorph, we conducted XRD analysis of three new samples that were extracted from the same Ketton limestone block. Figure S10 shows the comparison of the XRD spectra of a representative sample with the RRUFF reference of calcite, suggesting that Ketton is predominately composed of the calcite and that the needle-shaped particles are probably the pseudomorphs i.e., aragonite converted into calcite (Figure S8).

Next, the petrophysical properties of the four samples i.e., K1, K2, K3 and K4 were investigated through analysis of the initial XMT images and of the extracted pore networks for the initial conditions in the samples. The initial porosity of each sample was calculated by dividing the volume of pore space by the total volume of the sample. The initial permeability of each sample was calculated from the single-phase flow simulation on extracted pore networks. A comparison of the porosity of all samples shows that K1, K2 and K3 have similar initial porosity while K4 has a different initial porosity (Table 1).

Figure S11 shows the statistical distribution of some of the characteristic properties of the initial pore space of the samples. K1, K2 and K3 have similar throat radii and K2 and K3

have similar pore sizes. K4 has a slightly wider range of pore sizes and throat widths than K1-K3, while all four samples have a similar distribution of coordination numbers. Figure S11e shows the frequency distribution of the normalized velocity which was obtained by normalizing the velocity value of each throat (i.e., obtained from PNM) by the Darcy velocity. The Darcy velocity was obtained by dividing the flow rate with the cross-sectional area of the sample. The frequency distribution of normalized velocity indicated the probability of faster and slower velocity channels in comparison with the Darcy velocity. K2 and K4 have a somewhat greater number of fast channels as compared to K1 and K3. The observed velocity field in this study is similar to the previously reported velocity field for Ketton samples (Al-Khulaifi et al., 2017). Overall, the narrowness of the velocity channel suggested that all four samples have relatively similar initial pore structure (Figure S11e).

2.7 Quantification of the changed volume of calcite

$\Delta V^{n}_{Calcite,effluent}$, the cumulative value of changed amount of calcite volume (m^3), was obtained as:

$$\Delta V^{n}_{Calcite,effluent} = \frac{Q\, M_{calcite}}{\rho_{calcite}} \sum_{i=1}^{n} \Delta cCa^{i}\, (t^{i} - t^{i-1}) \tag{4}$$

where, n is the sampling steps, Q is the flow rate ($m^3\ s^{-1}$), $\rho_{calcite}$ is the density of calcite (2710 Kg m^{-3}), $M_{calcite}$ is the molecular mass of calcite (0.1 Kg mol^{-1}) and ΔcCa is the difference between outflow and inflow Ca^{2+} concentration (mol m^{-3}).

$\Delta V_{Calcite,XMT}$, the change in the number of solid voxels of XMT images in an experiment duration denoted by time t, is given as:

$$\Delta V_{Calcite,XMT} = V^{t}_{Calcite,XMT} - V^{t=0}_{Calcite,XMT} \tag{5}$$

Average reaction rate was calculated from the time-based evolution of the macroporosity as:

$$r_{calcite}(t) = \frac{\rho_{calcite}}{\Delta M_{calcite}} \frac{\Delta \emptyset_{XMT}\,(t)}{\Delta t} \frac{V_b}{A\,(t)} \quad (6)$$

where, $r_{calcite}(t)$ is the average reaction rate (mol m^{-2} s^{-1}), $\Delta \emptyset_{XMT}$ (t) is the change in the macroporosity of the sample between the scan time t as compared to the initial porosity, Δt (s) is the acquisition time of the image and A(t) (m^2) is the surface area obtained by adding up the voxel faces forming the boundary between solid and pore phase and V_b (m^3) is the total volume of the sample. It should be noted that above reaction rates are based only on macroporosity while neglecting the changes in the microporosity. Average reaction rates at different time steps of the experiment was calculated from the XMT images of the half-length sample. The average reaction rate at the beginning and at the end of the experiment was calculated from the XMT images of the cropped length sample. Note that the average reaction rate calculated from Equation 6 inherited an error depending on the time interval of scans used in the calculation (i.e., Δt). We observed that for the scan time interval used in this study, this error was around 20% (SI Section S4, Figure S12).

Equation 6 calculates the average reaction rate from the average macroporosity changes. Additionally, we have calculated local reaction rate as:

$$rz_{calcite}(z) = \frac{\rho_{calcite}}{M_{calcite}} \frac{\Delta \emptyset_{XMT}\,(z)}{\Delta t} \quad (7)$$

where, $rz_{calcite}(z)$ is local reaction rate (mol m^{-3}) calculated from the change in the slice-averaged porosity of the sample (i.e., Figure 4b) occurred in the experiment duration, Δt, and at a distance of z from the sample inlet.

In order to understand the coupling of transport and reaction times scales, we have defined two dimensionless numbers i.e., Peclet number and Damköhler number.

The Peclet number (*Pe*) compared the time scale of advection to that of diffusion and was defined as:

$$Pe(t) = \frac{U_{av}\,(t)\; l\,(t)}{D} \tag{8}$$

where, U_{av} (m s^{-1}) is the average pore velocity obtained by dividing constant Darcy velocity with the image-based porosity at different time steps, l is the mean pore radius calculated from the extracted pore network of the sample and D is the diffusion coefficient (3.36×10^{-9} $m^2\ s^{-1}$).

The Damköhler number (Da) compared the convection time scale with the reaction time scale:

$$Da(t) = \frac{rz_{calcite}\;\; MV_{calcite}}{A\;\; U_{av}\,(t)} \tag{9}$$

where, $MV_{calcite}$ is the molar volume of calcite (3.69×10^{-5} m^3 mol^{-1}), $rz_{calcite}$ indicates the reactive strength of the injecting acid (mol m^{-3} s^{-1}) at the inlet of the sample calculated from Equation 7 and A is the specific surface area of the cropped sample length at the beginning of the experiment.

The *Pe* and *Da* number, at different time steps were calculated from the XMT data of the half sample length, while, at the beginning and at the end of the experiment were calculated from the XMT data of the cropped sample length.

Experiment	**NCLS**	**LCLS**	**NCHS**	**HCHS**	**Method**
Ketton sample	K1	K2	K3	K4	-
Flow rate (m^3s^{-1})	4.16×10^{-9}	4.16×10^{-9}	4.16×10^{-9}	4.16×10^{-9}	-
Darcy velocity ($m\ s^{-1}$)	1.54×10^{-4}	1.54×10^{-4}	1.54×10^{-4}	1.54×10^{-4}	-
Injection duration (s)	72000	72000	43200	57000	-
Injected pore volume	6722	6977	3507	4489	-
Inflow pH(Calculated)	3.1	3.1	3.00	3.05	PHREEQC Pitzer
Inflow pH (Measured)	3.01	2.97	2.77	3.03[c]	pH electrode SenTix™or WTW
Inflow Ca^{2+} ($mol\ dm^{-3}$)	-	1×10^{-3}	-	335×10^{-3}	ICP-OES
Inflow -salinity ($mol\ dm^{-3}$)	0.2×10^{-3}	0.2×10^{-3}	1.16×10^{-3}	1.12×10^{-3}	ICP-OES
Inflow-saturation index (SI)	-	-11.45	-	-8.04	PHREEQC Pitzer
Porosity at t = 0s (%)	13.42	12.1	13.88	16.3	XMT [a]
Permeability (k_{PNM}) at t = 0s (m^2)	1.13×10^{-12}	6.37×10^{-13}	1.31×10^{-12}	3.18×10^{-12}	Flow simulation on cropped sample length using PNM
Permeability (k_{DNS}) at t = 0s (m^2)	1.98×10^{-12}	4.75×10^{-12}	1.77×10^{-12}	3.97×10^{-12}	Flow simulation on cropped sample length using DNS
Average equivalent diameter at t = 0s (m)	0.89×10^{-4}	0.53×10^{-4}	0.51×10^{-4}	0.65×10^{-4}	XMT [a]
Average volume of pores at t = 0s (m^3)	0.57×10^{-11}	0.29×10^{-11}	0.31×10^{-11}	0.47×10^{-11}	XMT [a]
Number of pores in the extracted pore network	6832	6259	6948	6130	PNM[b]
Number of throats in the extracted pore network	12419	10915	12919	10919	PNM[b]
Average pore radius at t = 0s (m)	5.46×10^{-5}	4.97×10^{-5}	4.93×10^{-5}	5.31×10^{-5}	PNM[b]
Average throat radius at t = 0s (m)	2.59×10^{-5}	2.61×10^{-5}	2.59×10^{-5}	2.93×10^{-5}	PNM[b]
Average coordination number at t = 0s	3.64	3.49	3.72	3.56	PNM[b]
Average pore velocity at t = 0s ($m\ s^{-1}$)	2.43×10^{-5}	2.79×10^{-5}	2.47×10^{-5}	2.47×10^{-5}	PNM[b]
Size of the full sample length (Voxels)	1319×1317×2494	1316×1316×2418	1317×1319×2552	1317×1318×2342	XMT Images

Size of the cropped sample length (Voxels)	1319×1317×1950	1316×1316×1950	1317×1319×1950	1317×1318×1850	XMT Images
Size of the half sample length (Voxels)	1319×1317×818	1316×1316×850	1317×1319×850	1317×1318×782	XMT Images
Scan interval of the half sample length (min)	40,136, 154, 154, 154, 154, 154, 154	90, 90, 90, 99, 105, 120, 126	150,30,180,120,120,160,136,56	40,215,20,75,165,165,165,165,165,25	-

Table 1: Parameters for all four dissolution experiments including the skeleton (pore network) information. [a] XMT image of cropped sample length. [b] Pore Network Model of cropped sample length. [c] pH measurements were done on a separate solution made according to the same recipe and using a WTW – Sensolyt 900-P pH electrode; for this solution, the SenTix electrode was affected by the high concentration of ions in the solutions.

3. RESULTS AND DISCUSSION

This study is based on four reactive flow experiments (Table 1 and Table S1): NCLS (No Calcium Low Salinity), LCLS (Low Calcium Low Salinity), NCHS (No Calcium High Salinity) and HCHS (High Calcium High Salinity). The analysis of effluent solution for all four experiments is provided in Section 3.1.1. The results are compared with the XMT image-based analysis in Section 3.1.2. Next, we assess the temporal evolution of bulk porosity and local porosity in Section 3.1.3 and corresponding effective reaction rate in Section 3.1.4. Further, we examine the characteristics of the dissolution structures developed in each experiment in Section 3.2. Finally, the impact of the dissolution structures on permeability changes is provided in Section 3.3.

3.1 Mass transfer analysis

3.1.1 Effluent Analysis

Figure 1a presents the temporal evolution of the normalized Ca^{2+} concentration (ΔcCa), which represents the difference between outflow and inflow Ca^{2+} concentration during the sampling interval. Positive values of ΔcCa for experiments NCLS, LCLS and NCHS indicates persisting dissolution throughout the experiments. From the first sampling point onwards, the experiment NCLS maintained a steady-state value of outlet Ca^{2+} concentration and ΔcCa. Experiment LCLS, on the contrary, initially provided a lower outflow concentration compared to NCLS, which later approach towards a higher steady-state value. For experiment NCHS, outflow Ca^{2+} concentration showed a decreasing trend. From the saturation index of the injected solutions, we estimated the maximum amount of Ca^{2+} concentration which could be dissolved before these solutions would reach equilibrium with respect to calcite. Comparison of these estimates with the measured ΔcCa suggests that the outflow solutions of experiments NCLS, LCLS and NCHS were almost in equilibrium with

calcite (Figure 2a). Note that, the differences between the quantities of dissolved Ca^{2+} ions observed in the experiment and those in the simulation most likely reflect the impact of differences in sample's initial permeability on the overall amount of calcite dissolved during the experiments. Future investigations on homogenous porous media (e.g., 3D-printed) could circumvent such uncertainties.

In the case of experiment HCHS, normalized ΔcCa was negative initially, followed by positive values (Figure 1a). As stated earlier, the inflow solution HCHS was acidic, with the measured pH value of 3.05, and undersaturated with respect to the calcite. Through the examination of mixing calculations (specifically, PHREEQC + Pitzer calculations when mixing varying fractions of inflow solution HCHS with a solution in equilibrium with calcite), we did not identify any ratios resulting in either supersaturated mixtures or salting-out conditions. Moreover, from the saturation index, we estimated that this solution can dissolve up to around 0.7×10^{-3} mol dm^{-3} calcite, before reaching equilibrium with respect to calcite (Figure 2a). Therefore, it is most likely that the initial negative ΔcCa value does not represent calcite precipitation but was caused by error accumulation during the strong dilution necessary on in- and outflow samples in preparation of ICP-OES measurements from which ΔcCa values were calculated. We suspect the calculated Ca^{2+} concentrations for HCHS samples included an uncertainty larger than the standard error of 10% (SI Section S5.1, Figure S13).

We observed the impact of salinity and Ca^{2+} concentration of the inflow solutions on the equilibrium concentrations (Figure 2a). As expected, inflow solutions containing Ca^{2+} ions (i.e., LCLS and HCHS) required a lower amount of Ca^{2+} ions to reach to the equilibrium as compared to the inflow solutions with no Ca^{2+} ions (i.e., NCLS and NCHS) (Figure 2a). Similarly, increments in salinity led to enhanced solubility of calcite, with more saline inflow

385 solutions dissolving larger amounts of calcite than the inflow solutions with lower salinity
386 (i.e., NCLS) (Figure 2a).

387 Figure 1b shows the measured pH of the effluent samples from all four experiments. Inflow
388 solutions all had an approximate pH value of 3.0 (Table S1). The higher pH values measured
389 in the outflow indicate dissolution-induced solution buffering. The amount of fluid buffering
390 directly relates to the amount of Ca^{2+} ions produced (Figure 1). Initially, experiment NCHS
391 showed both the highest value of pH and Ca^{2+} concentration at the outflow, followed by a
392 decreasing trend (Figure 1). For experiment NCLS, outflow pH remained constant and for
393 experiment LCLS, outflow pH showed an increasing trend. We observed a good agreement
394 between the measured outflow pH and predicted outflow pH (Figure 2b). For the experiment
395 HCHS, the pH of the outflow solution was calculated corresponding to the equilibrium
396 concentration. For this experiment, we observed a higher difference between the calculated
397 pH and the measured pH (Figure 2b). This is probably due to the higher uncertainty
398 associated with the pH measurement in highly saline Ca^{2+}-rich outflow solution.

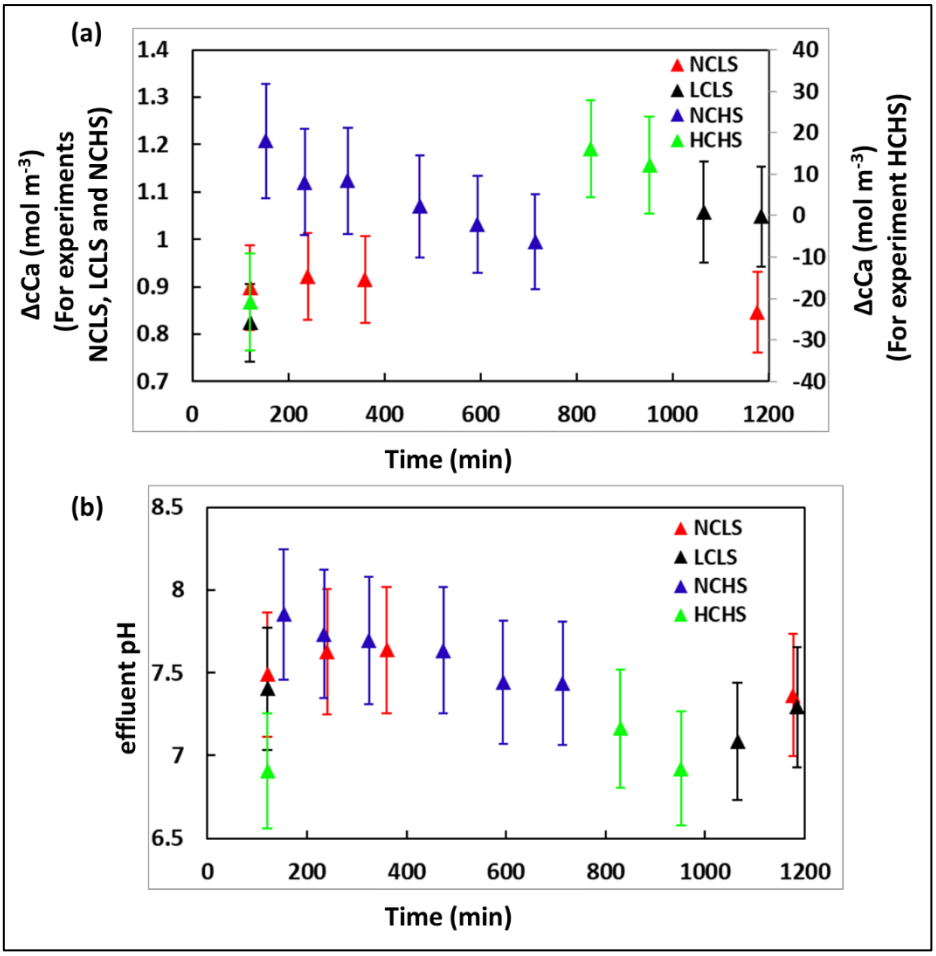

399

400 **Figure 1: (a) Measured Ca^{2+} concentrations from effluent solution for experiments**

401 **NCLS, LCLS, NCHS (left-hand vertical axis) and HCHS (right-hand vertical axis) (b)**

402 **Measured pH from effluent solution for all four experiments**

403

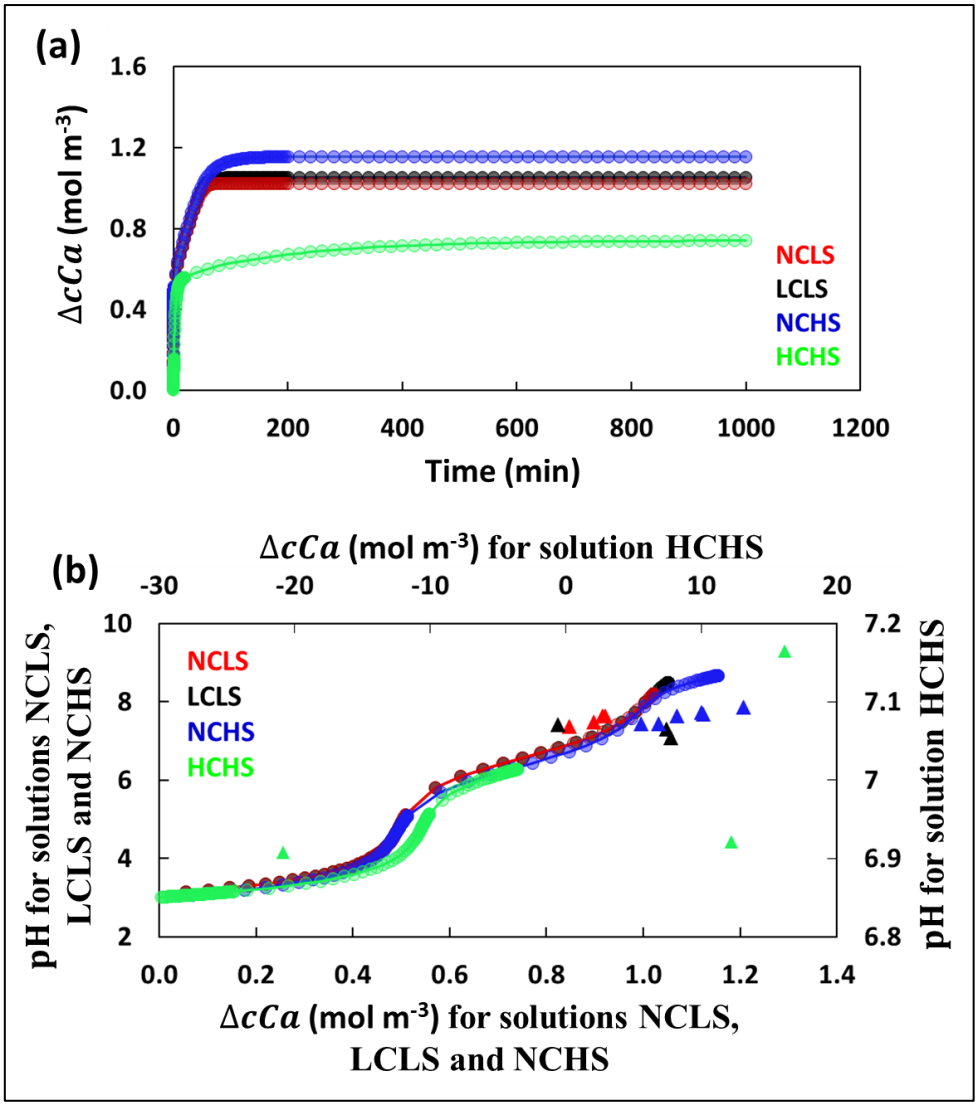

404

405 **Figure 2: PHREEQC simulations for all four injected solutions showing (a) the**
406 **maximum amount of ΔcCa which can be dissolved before the solution reaches to the**
407 **equilibrium and (b) pH of the solution as a function of the added amount of ΔcCa.**

408

409 **3.1.2 Effluent concentrations vs XMT Analysis**

410 The comparison of the calcium concentration in the effluent with ketton volume (loss) with
411 XMT helps to (further) quantify the amount of dissolution in the different experiments.
412 Figure 3a shows a comparison of the changed amount of calcite volume, calculated using
413 ΔcCa with values obtained from XMT image analysis using Equations 4 and 5, respectively.
414 For experiments NCLS, LCLS and NCHS, we observed a difference of ~around 14-25%

between values obtained from effluent analysis and those from XMT images (Figure 3a). A potential cause of this discrepancy could be resolution of imaging (voxel size 6 μm). This difference would be dependent on the length of the sample along the flow direction used in volume change calculations. Increased difference for cropped length sample-based analysis, as shown in Figure 3a, is due to dominance of dissolution close to the sample inlet. As discussed in Section 2.3, the remaining part of this study will be based on the analysis of the cropped length sample. Figure S5 shows the cropping position through a vertical slice of sample K1. It should be noted that while the calculated mass of dissolved calcite from the effluent and XMT analyses doesn't exhibit an exact correspondence, they do, in essence, agree on the relative extent of dissolution rate among the NCLS, LCLS, and NCHS experiments.

For experiment HCHS, the difference between effluent analysis and XMT images was more significant (Figure 3a). This, along with the arguments provided in Section 3.1 further suggests that the ICP-OES measurement of solutions containing a high amount of Ca^{2+} ions might have inherited higher uncertainty.

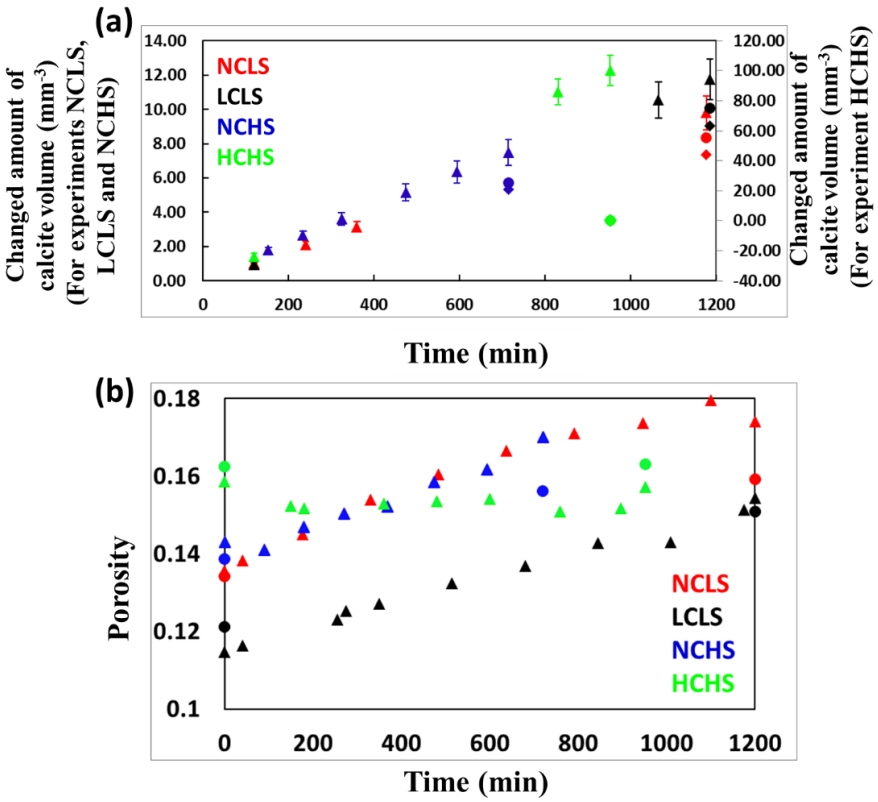

Figure 3: (a) Cumulative changes in the solid calcite volume calculated from effluent analysis (triangle) and using XMT images (circle, full sample length and diamond, cropped sample length) for experiments NCLS, LCLS, NCHS (left-hand vertical axis) and HCHS (right-hand vertical axis). (b) temporal evolution of the macroporosity calculated from XMT images (circle, cropped sample length and triangle, half sample length) for all four experiments.

3.1.3 Porosity

The time-lapse imaging of the sample allowed *in situ* tracking and analysis of the dissolution-induced changes in the porosity. Figure 3b shows the temporal evolution of macroporosity during the four experiments calculated from XMT images. Injection of undersaturated solutions led to an increase in the macroporosity of samples for experiments NCLS, LCLS, and NCHS. Consequently, total increments in the macroporosity are of magnitudes 0.025,

443 0.0296 and 0.0158 for experiments NCLS, LCLS, and NCHS, respectively. It should be
444 noted that the observed reduction in porosity in the NCLS experiment towards the end could
445 potentially be attributed to the clogging of certain pores by migrating calcite particles after
446 detachment due to dissolution of some of the matrix.

447 For the experiment HCHS, macroporosity of the top half of the sample first slightly
448 decreased and then this decreased macroporosity was nearly maintained until the end of the
449 experiment, where a slight increment was observed (Figure 3b). Luquot et al., 2014 has also
450 observed similar decrement in the macroporosity for the acids with lower corrosiveness (i.e.,
451 less strong undersaturation). They noted that the acids with lower reactive strength attack the
452 microporosity of the grain and resultant small particles clog the macropores. The change in
453 macroporosity obtained from XMT images does not resolve such changes in microporosity.
454 Therefore, changes in the microporosity of the sample were investigated through changes in
455 grey volume in the full samples between beginning and end of the experiment (SI Section
456 S5.2). For the same sections of the sample (i.e., cropped sample length) of this experiment,
457 we observed that the total change in the grey volume (i.e., microporosity + macroporosity)
458 was 3.3 $\times 10^{-9}$ m^3 as compared to the segmented volume (i.e., macroporosity) of a value of
459 0.16 $\times 10^{-9}$ m^3 (Figure S14: semi quantitative). This suggests that the inflow solution HCHS
460 had dissolved more sub-resolution calcite matrix and the detached fine grains accumulated in
461 the macropores (cf. Luquot et al., 2014).
462 Figure 4 provides a vertical profile of porosity along the direction of the flow. Each data
463 point was obtained by averaging using a moving windows including 30 consecutive 2D slices
464 (i.e., corresponding to 0.18mm). Comparison of the vertical porosity profile of the samples
465 from the initial and final time steps of the dissolution experiment unveiled the following
466 information:

Firstly, for experiment NCLS, we observed a strong deviation of evolved porosity distribution along the flow path compared to initial porosity distribution whereas, for experiment LCLS and NCHS, evolved porosity distribution was similar to initial porosity distribution (Figure 4a). This is caused by the difference in reactive strength of the injecting fluid, as also discussed Section 3.2.1.

Next, we observed that solution NCLS created maximum porosity changes in the first 2 mm part of the sample whereas for solution LCLS, the effective depth of reaction front (i.e., corresponds to a porosity difference (new porosity (%) - old porosity (%) of more than 3%) was around 5mm (Figure 4b). In the case of solution NCHS, the top 3mm part of the sample experienced an average of 3% porosity change. The depth of penetration of the reaction front is related to the amount of fluid buffering. Fluid buffering is a result of a complex interplay of initial reactive strength of the injecting fluid and transport time scale (e.g., Agrawal et al., 2020; Gray et al., 2018; Molins et al., 2014). Section 3.1.4 explores this relationship between reaction and transport time scale for an individual experiment. For experiments NCLS, LCLS, and NCHS, the whole sample showed positive porosity changes, whereas, for experiment HCHS, the top part of the sample showed negative porosity changes (Figure 4b). It is worth noting that for experiment HCHS, % macroporosity difference is less than 0.5% and that dissolution in micropores played an important role. Alternatively, the SI values obtained with our generalized Pitzer model may be inaccurate (Harvie and Weare, 1984; Felmy and Weare, 1986), and locally calcite supersaturation may have occurred, leading to the observed pore clogging/porosity decrease.

Note that, due to the constraints with the data acquisition as mentioned in Section 2.2, bulk porosity for the first- and last-time steps of the experiment was calculated from the data of the full sample (Figure 3b). However, porosity for the intermediate time steps was calculated from the data of half-length sample i.e., part of the sample near the injection point. The

492 difference between porosity data of these two samples size at time t= 0 denotes the initial
493 heterogeneity of the samples (Figure 4a) whereas, the difference at the end of the experiment
494 is a result of dissolution heterogeneity along the direction of flow (Figure 4b).

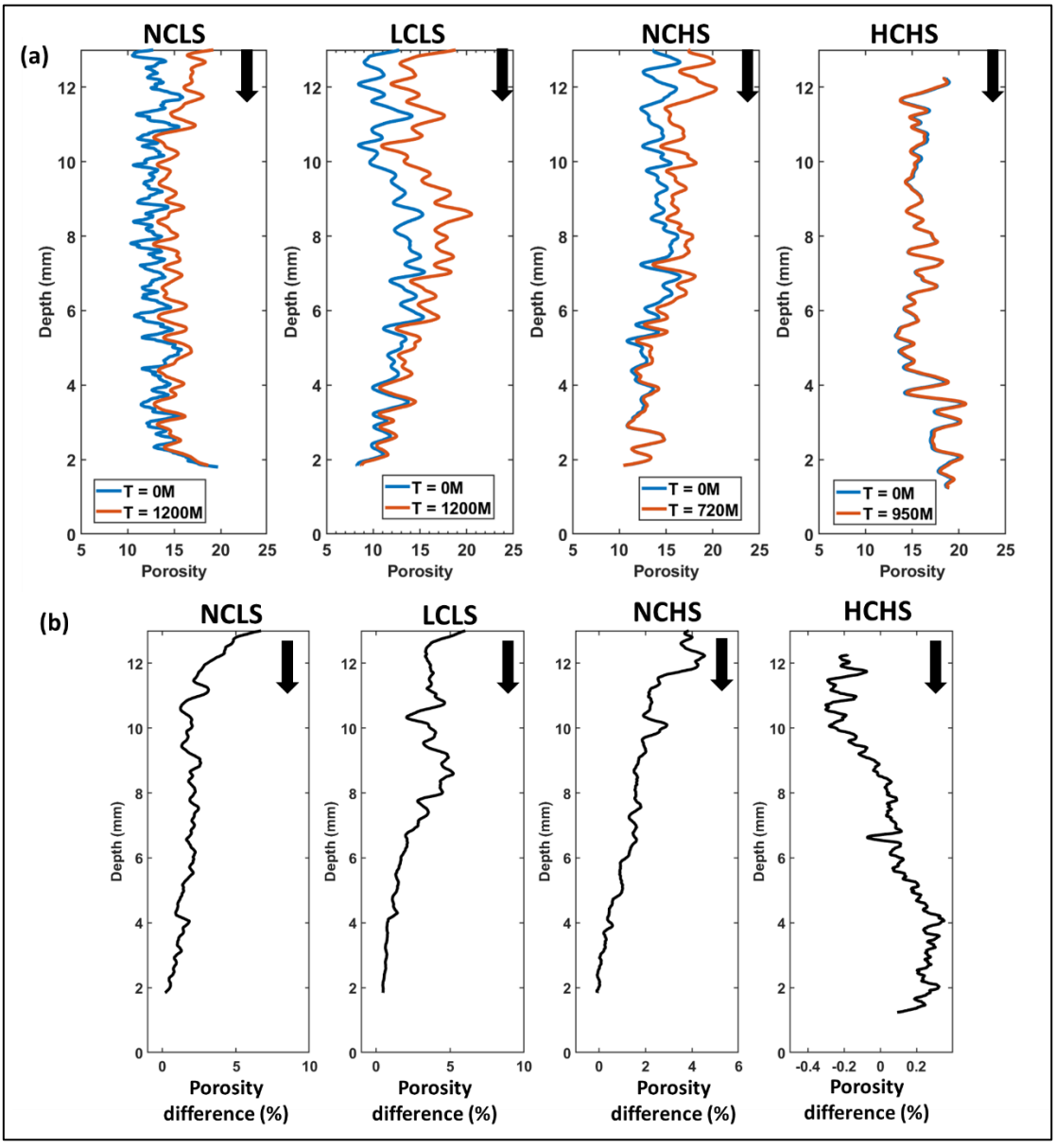

495

496 **Figure 4: Porosity changes in all four experiments showing (a) the slice-averaged**
497 **porosity values (%) along the sample, and (b) difference between porosity values (%).**
498 **The vertical profiles corresponded to the XMT images of the cropped sample length at**
499 **the beginning and the end of experiment. In order to increase the visibility, only a part**
500 **of the vertical profile (i.e., from 1.8 till 12.5 mm) is shown. Figure S15 shows the full**

vertical profile (i.e., from 1.8 mm till 13.5 mm). Black arrow indicates the flow direction. Note the different x-axis ranges utilized for panel (b). Note that flow was established from bottom to top of the sample and all presented images are upside down.

3.1.4 Reaction rate and dimensionless numbers

Time-lapse XMT scans of the sample enabled monitoring of the macroporosity of the sample as the experiment progressed. This porosity was utilized to obtain the changed amount of calcite mass to calculate the evolution of the average reaction rate over the course of the experiments. Figure 5a shows the evolution of the average reaction rate for all four experiments. Figure 6 shows the vertical profile of the local reaction rate calculated from the XMT images of the full sample obtained at the beginning and the end of the experiment.

We observed that the addition of the Ca^{2+} ions in the inflow solution decreased the calcite dissolution rate (NCLS vs LCLS and NCHS vs HCHS in Figures 5a and 6). For example, at 40 minutes, the average dissolution rate corresponding to the NCLS solution was 47.3% higher than the solution LCLS. Similarly, the solution NCHS (i.e., no Ca^{2+} ions and high salinity) also showed a higher average dissolution rate as compared to the solution HCHS (i.e., 337×10^{-3} mol dm^{-3} Ca^{2+} ions and high salinity). In the past, several studies have shown such inhibitory impact of the Ca^{2+} ions over the calcite dissolution kinetics (Buhmann and Dreybrodt, 1987; Sjöberg and Rickard, 1985).

We observed that the dissolution rate of macroporosity at the sample inlet for solution NCHS was approximately 54% less than solution NCLS (refer to Figure 6). Additionally, the mean dissolution rate of macroporosity, calculated over half the sample length, was found to be lower in experiment NCHS compared to NCLS (see Figure 5a). Prior effluent analysis revealed higher outflow Ca2+ concentrations in experiment NCHS than in NCLS (Figure 1a). A plausible justification is the conflicting impacts of salinity on the dissolution rate and the

525 solubility of calcite. In saline solutions, the dissolution rate might be hindered, but the
526 solubility of calcite might be enhanced. Consequently, saline solutions, despite exhibiting
527 diminished macroporosity-based dissolution rates near the sample inlet, were able to dissolve
528 more calcite across the entire sample length before reaching equilibrium with calcite. Another
529 possible explanation is that a higher dissolution rate in microporosity regions in the NCHS
530 experiment compared to NCLS experiment is currently not reflected in the calculated
531 dissolution rates.

532 The *Pe* number for all four experiments was greater than one, indicating advection-controlled
533 transport regimes such that the rate of renewal of the fluid inside pore space of the sample
534 was dominated by advection (Figure 5b). For all experiments, the *Da* number was less than
535 1.0. This suggests that the dissolution conditions in the sample were reaction-limited
536 (Figure 5c) as the time scale of advection is shorter than that of dissolution reaction. As the
537 experiment progressed, we observed a decrease in the Pe number. This is because wormholes
538 are dominantly responsible for porosity changes and average pore size did not increase by the
539 same proportion as porosity increased.

540 For the studied reaction-controlled dissolution regime, this decrease of the *Pe* number also
541 contributes to a decrement in the average dissolution rate (Figure 5a). This impact of the
542 temporal evolution of the *Pe* number over the average dissolution rate was much clearer in
543 experiment NCLS compared to LCLS and NCHS experiments.

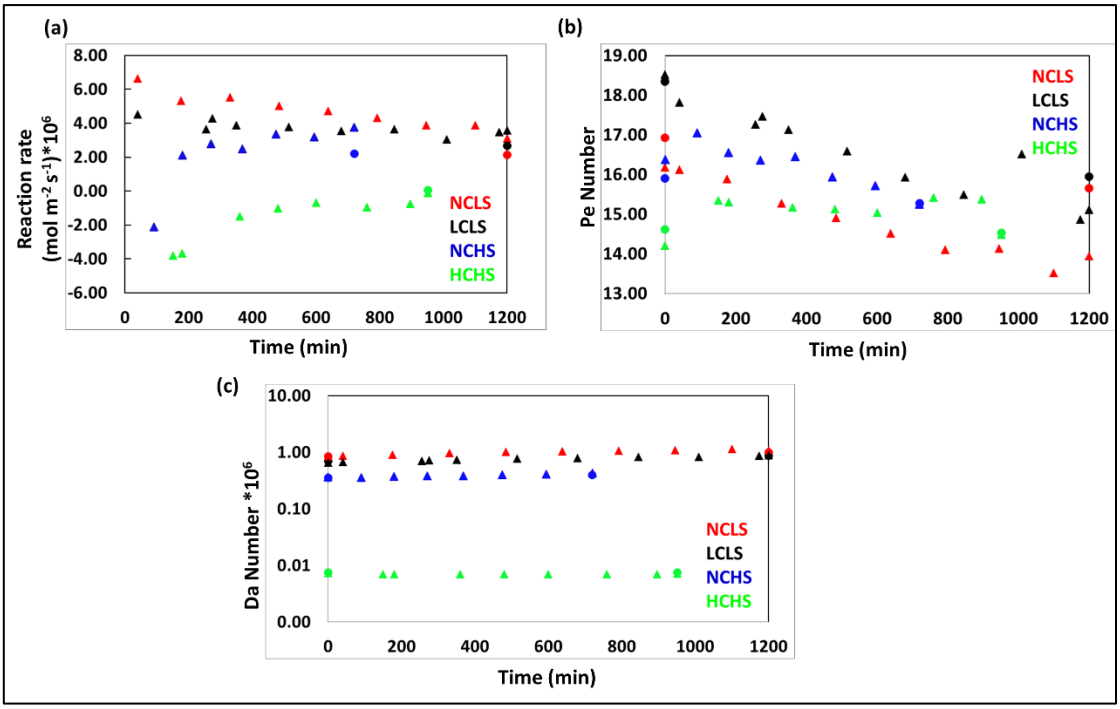

544

545 **Figure 5: Temporal evolution of (a) the average reaction rate based on Equation 6, (b)**
546 ***Pe* Number, and (c) *Da* number, calculated from XMT images (circle, cropped sample**
547 **length and triangle, half sample length).**

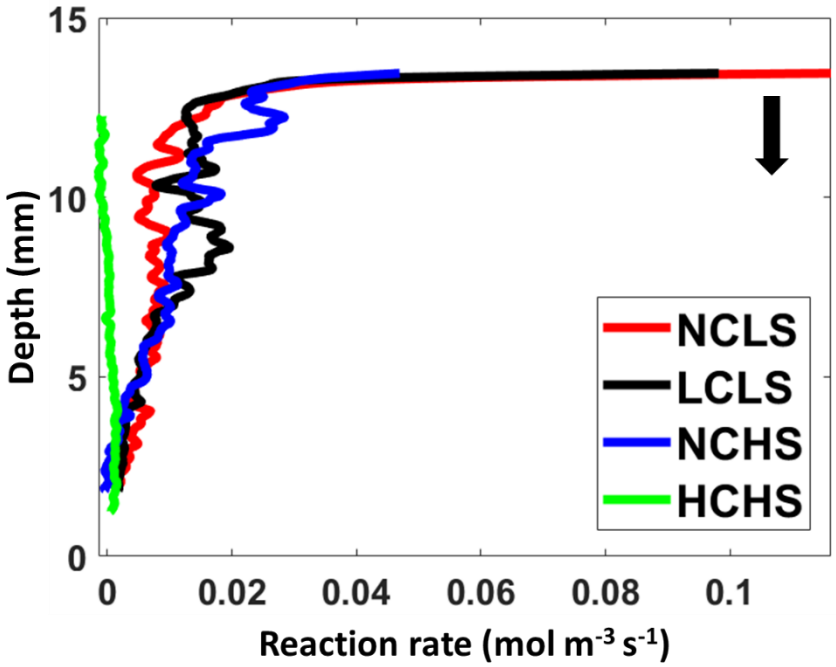

548

549 **Figure 6: The full vertical profiles of the slice-averaged dissolution rate for all four**
550 **experiments calculated using Equation 7. The black arrow indicates the flow direction.**

3.2 Evolution of the dissolution structure

All four experiments were performed with the same injection rate and on samples from the same rock type with very comparable pore structure (Figure S11). Therefore, as expected, the reactive strength of the injecting solutions was directly reflected by the *Da* number. The *Da* number is highest for experiment NCLS, then LCLS, NCHS, and HCHS. Previously, the control of the *Da* number on the dissolution patterns has been investigated through both experimental and numerical studies (Fredd and Fogler, 1998; Golfier et al., 2002; Hoefner and Fogler, 1988; Luquot et al., 2014; Maheshwari et al., 2013). Table 2 provides overview of the dissolution patterns observed in the previous studies. In the next sections, we discuss the qualitative and quantitative aspects of the dissolution patterns developed in each experiment.

Sample rock	Pe	Convective Da	Type of Dissolution	Reference
NaCl Salt grains packed porous media	8.32×10^{-4}	120	Face dissolution	Golfier et.al., 2002
	4.14×10^{-3}	24	Conical wormhole	
	1.66	6.01×10^{-2}	Dominant wormhole	
	83.2	1.2×10^{-3}	Ramified wormhole	
	832	1.2×10^{-14}	Uniform dissolution	
Oolitic grainstone from the Lusitanian Basin	0.2	$0.1\text{-}1 \times 10^{-4}$	Dominant wormhole and uniform dissolution	Luquot et.al., 2014
Ketton carbonate rock	9	0.5	Dominant wormhole	Gray et.al., 2018
Ketton carbonate rock	2100	2.8×10^{-5}	Uniform dissolution	Menke et.al., 2015
Ketton carbonate rock	14-19	7.28×10^{-9} - 8.53×10^{-7}	Dominant wormhole – Uniform dissolution	This study

Table 2: Overview of the dissolution pattern observed in the previous studies.

3.2.1 Dissolution structures in experiments NCLS, LCLS and NCHS

564 Experiment NCLS was performed with a solution that has low salinity, devoid of Ca^{2+} ions.
565 This injected solution initiated the dissolution with an effective reaction rate of a magnitude
566 of 7×10^{-6} mol m^{-2} s^{-1} (Figure 5a). Addition of a small amount Ca^{2+} ions (experiment LCLS),
567 lowered initial effective reaction rate to 4×10^{-6} mol m^{-2} s^{-1} (Figure 5a). In the experiment
568 NCHS, injection of a saline solution that did not contain Ca^{2+} ions, caused a lower dissolution
569 rate than in experiments NCLS and LCLS (Figure 5a and 6).

570 The time-lapse scanning of the pore space allowed a qualitative analysis of the temporal
571 evolution of the dissolution structures in these experiments. In experiment NCLS, it was
572 noted that dissolution was remarkably uniform in the radial direction during the initial 40
573 minutes (Figure 7a), indicating that the initial phase of dissolution was primarily influenced
574 by fluid acidity rather than the sample's initial pore structure (Figure 7a). Such difference
575 between the modified porosity and the initial porosity was also clear in the vertical porosity
576 profiles provided in Figure 4a. The radially homogeneous dissolution occurred in the first
577 ~2mm of the flow path, after which selective dissolution paths continued further along the
578 flow direction (Figure 7a). This development of dissolving channels was most likely guided
579 by the initial heterogeneity and structure of the sample. Conversely, for experiments with
580 lower Da numbers (i.e., LCLS and NCHS the formation of the dissolution structure was more
581 significantly influenced by the heterogeneous pore structure of the sample, as contrasted with
582 experiment NCLS (Figure 7b-c, and 4a). For example, in the experiment LCLS, after 40
583 minutes of acid injection, dissolution created sparsely localized flow channels (Figure 7b).
584 From the scans of the half sample length, we observed that the sample's pore space evolved
585 into several conducting channels. The trajectories and length of these channels were
586 established within a certain experiment duration (i.e., 484 minutes in experiment NCLS, 255
587 minutes in experiment LCLS and 369 minutes in experiment NCHS) while the diameter of
588 channel continued to grow (Figure 7 and S16). From the scan of the full sample, which was

589 acquired at the end of the experiment (i.e., 1200 minutes for the experiments NCLS and
590 LCLS; 720 minutes for the experiment NCHS), we observed that most of these channels did
591 not develop much beyond the half sample length that was scanned during the experiment
592 (Figure 8). In the experiment NCLS, two of the channels extended over the full length of the
593 sample, while in the experiments LCLS and NCHS, only one such dominant channel was
594 formed (Figure 8).

595 Next, through skeleton analysis, we characterized and quantified final form of the dissolution
596 structures in these three experiments (Figure S17; Table S2). The quantification was based on
597 attributes derived from the individual segments of the channels and side branches: the length
598 (sum of the segment length), radius (radius of the segments) and mean radius (average of the
599 segment radius).

600 The evolution of the dissolution structures also indicates that the less reactive injecting
601 solutions (i.e., higher Ca^{2+} and/or salt concentration) resulted in localization of the channels.
602 This was evident from the decreasing number of inlet nodes (where the number of inlet nodes
603 shows unique/main flow channels) with the decreasing Da number (Table S2). All the
604 channels originating from the inlet nodes were divided into three categories based on their
605 lengths (Figures S18-S20; Table S2). Figure S21 shows the histogram of the channel lengths
606 for experiments NCLS, LCLS and NCHS. We observed that in the experiment NCLS, two
607 dominant channels of a length ~14 mm were formed. In contrast, in the experiments LCLS
608 and NCHS, only one dominant channel of the length of 12.30 and 10.28 mm, respectively,
609 was formed.
610 The impact of the reactivity of the injected solution on the starting diameter of the channel
611 was also observed (i.e., in the vicinity of the sample inlet). For example, in the experiment
612 NCLS, the starting diameter of two of the category 1 channels was larger than 0.6 mm while,
613 in the experiments LCLS, the starting diameter of both of the category 1 channels was

smaller than 0.4 mm (Figure S22a and b). Moreover, the *Da* number also represents the buffering of fluid as it moves along the sample (Agrawal et al., 2020). This is reflected in the vertical radius profile (i.e., in the direction of flow) of the channels. In the experiments LCLS and NCHS, the vertical radius profiles of the category 1 channels were more homogeneous than the experiment NCLS (Figure S22).

Furthermore, in the experiment LCLS, for each category 1 channel, the number of side branches and the length of the side branches were significantly higher than the experiment NCLS (Table S2, Figure S23a-b and S24a-b). The increased ramification of dissolution channels with decreasing *Da* number has also been observed by Luquot et al. (2014). On the contrary, the dissolution pattern in the experiment NCHS developed with the least amount of ramification as evident from the least number of end nodes (Table S2, Figure S23c).

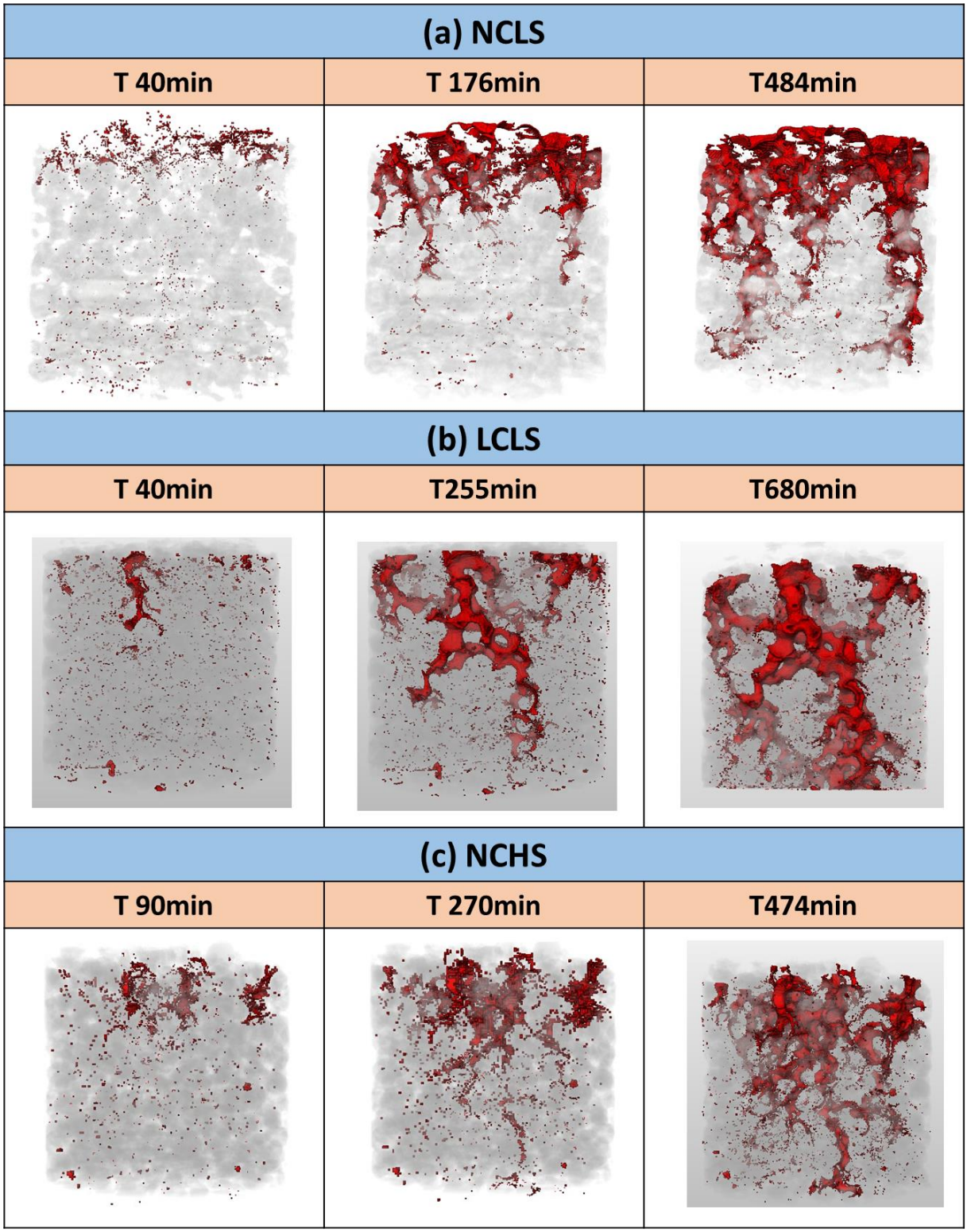

628

629 **Figure 7: Temporal evolution of the dissolution patterns in experiment (a) NCLS, (b)**
630 **LCLS and (c) NCHS. XMT images of these samples at the remaining time steps are**
631 **shown in Figure S16.**

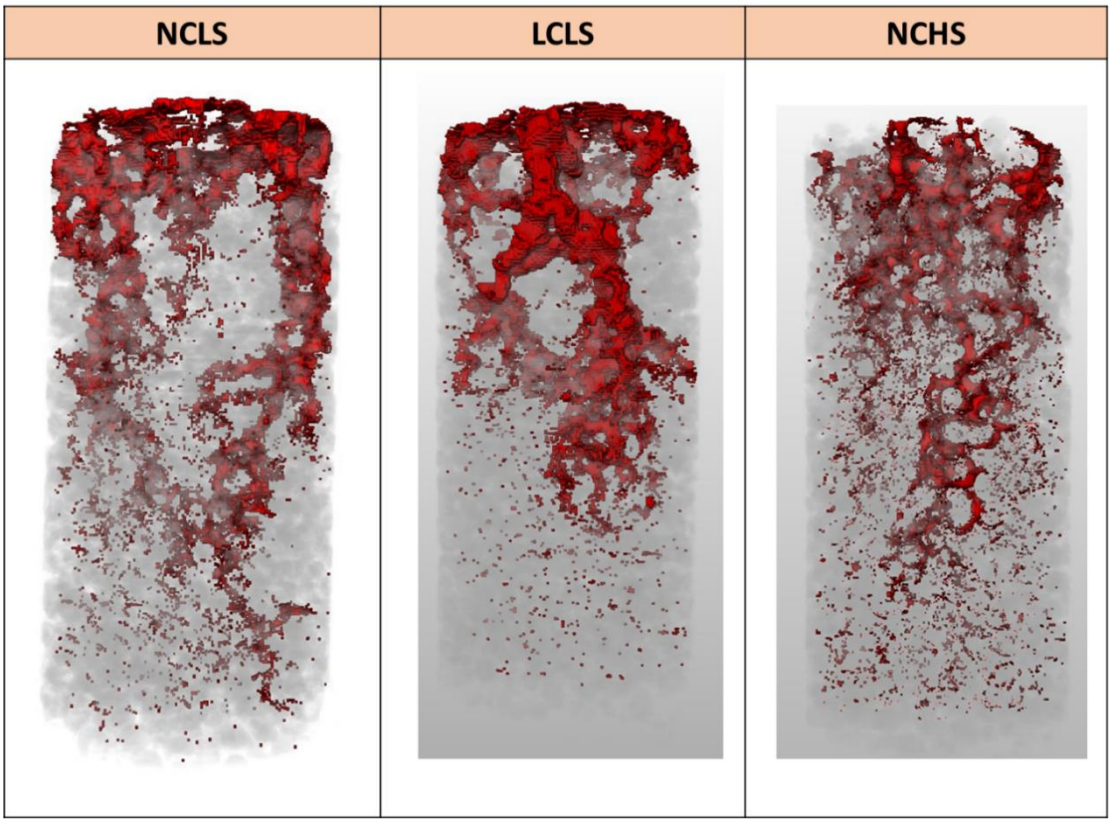

Figure 8: Final form of the dissolution patterns in experiments NCLS, LCLS and NCHS. Note that the duration of experiments NCLS, LCLS and NCHS was 1200, 1200 and 720 minutes.

3.2.2 Experiment HCHS

We observed that the presence of a high amount of Ca^{2+} ions lowered the effective dissolution rate by two orders of magnitude compared to experiment NCHS (Figure 5a). As mentioned earlier, the macroporosity of the top part of the sample decreased throughout this experiment (Figure 3b and 4). Figure 9 presents the temporal evolution of the pore space where the locations of removed solid mass and of added solid mass are highlighted. As explained earlier, the injected HCHS was acidic and undersaturated with respect to the calcite and mixing calculations (performed in PHREEQC with default Pitzer database) showed that it is unlikely that mixing variable amounts of the HCHS solution with the equilibrated initial solution present in the sample can result in a composition that is supersaturated with respect

646 to calcite. A possible explanation of the accumulated solid mass in the pore space is related to
647 the dissolution of the microporous matrix, causing solid particles to detach from the matrix
648 and migrate through the pore space. This is described by the so-called sugar lump model
649 (Luquot et. al., 2014). From the XMT image after 150 minutes of acid injection, we observed
650 that small amounts of such displaced particles were uniformly distributed in the pore space
651 (blue in Figure 9). Dissolution of the microporous matrix was confirmed by grey value
652 analysis of the images (Figure S14; semi quantitative), which showed an increase in the sum
653 of microporosity and macroporosity. From the scan of the full sample at the end of the
654 experiment (Figure 9c), we observed that the amount of clogging by displaced solid particles
655 was higher closer to the inlet. This is consistent with most of the dissolution occurring closer
656 to the inlet, also in the microporous domain, leading to more detachment and local
657 displacement of particles. Alternatively, use of the default Pitzer model in PHREEQC for the
658 calculation of the solution chemistry might have led to an overestimation of the
659 undersaturation state of the inflow solution (Harvie and Weare, 1984; Felmy and Weare,
660 1986) and locally calcite supersaturation may have occurred, leading to the observed pore
661 clogging.

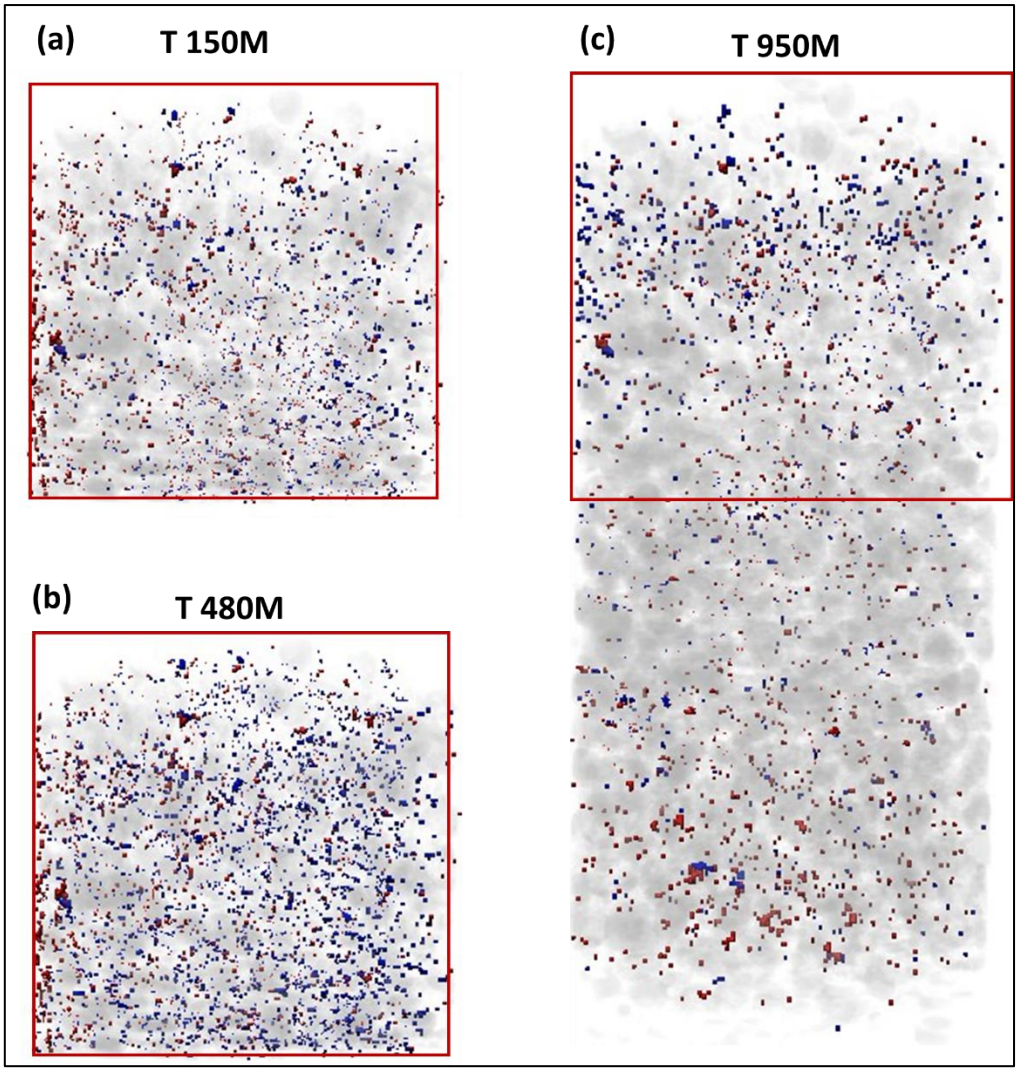

Figure 9: Temporal evolution of the pore space in the experiment HCHS. Red colour highlights the locations from where the solid mass was removed. Blue colour highlights the locations where the solid mass was added. XMT images of this sample at other time steps are shown in Figure S25. Note that red coloured box shown in plot (c) indicates the volume imaged in plots (a) and (b).

3.3 Evolution of transport properties

Dissolution patterns control permeability changes in the sample, which is related to the volume of acid injection required for wormhole breakthrough (PV_{BT}). One of the earlier definitions of wormhole breakthrough is when the permeability of the sample increases by a

672 factor of 100 (Fredd and Fogler, 1998). The amount of acid required for a breakthrough is a
673 function of the dissolution pattern, and therefore depends on *Pe* and *Da* numbers, which
674 reflect the injection rate and the solution's corrosive nature (i.e., chemical reactivity, in the
675 current case determined by salinity and calcium concentration). For example, face dissolution
676 will require higher volumes of acid to attain a certain permeability increment than
677 wormholes.

678 Figure S26 shows the temporal evolution of permeability calculated from both the pore
679 network model and direct numerical simulation during all four experiments. For all
680 experiments, both methods yielded a similar amount of permeability change - i.e., a
681 noticeable permeability increment in the experiments NCLS, LCLS, and NCHS, and no
682 significant permeability change in experiment HCHS.

683 If we consider the definition of breakthrough from Fredd and Fogler (1998), none of the
684 experiments in this study led to a breakthrough point (Figure S27). The highest permeability
685 increment corresponding to a factor of 7.9 and 5.8 was noted for experiment LCLS based on
686 permeability values from the pore network model and direct numerical simulations,
687 respectively. We observed that the injection of the same number of pore volumes resulted in
688 the highest permeability increment for experiment LCLS and lowest for experiment HCHS
689 (Figure S27). This indicates that the dissolution pattern formed in experiment LCLS is
690 optimal, just as the *Da* number of this experiment is ideal among all four experiments.

691 The volume of acid required for a breakthrough was calculated through the extrapolation of
692 the direct numerical simulation-based permeability response curve as shown in Figure S27.
693 Figure 10 shows the distribution of PV_{BT} as a function of *Da* number. As expected for
694 experiment LCLS, the lowest amount of pore volumes was required to achieve an increase in
695 permeability by a factor of 100. This suggests that the increasing amount of salinity and Ca^{2+}

696 concentration of the injecting solution results in an increase in the number of acid pore
697 volumes required for changing the permeability.

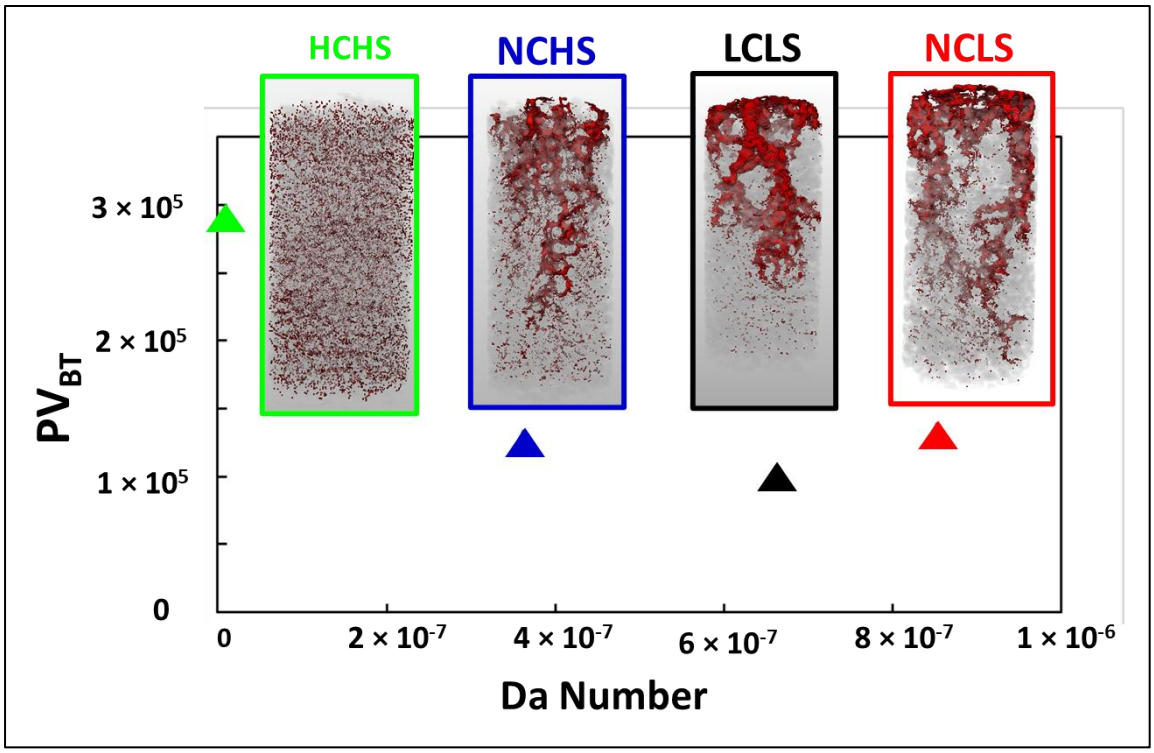

698

699 **Figure 10: The expected number of pore volumes to obtain a full breakthrough curve at**
700 **different *Da* number. Note that direct numerical simulation permeability, k_{DNS}, was**
701 **used for the calculation of PV_{BT}.**

702 Figure 11 shows the changes in permeability as a function of porosity for all four
703 experiments. In the past, several experimental and modelling studies have used the simplified
704 version of Kozeny -Carman relation i.e., a power-law relation as $k \sim \phi^n$, to relate the
705 permeability changes with the evolving porosity of the sample (e.g. Bernabé et al., 2003;
706 Luquot et al., 2014; Luquot and Gouze, 2009; Nogues et al., 2013; Pereira Nunes et al.,
707 2016). The exponent n is a function of the initial porous medium properties and the
708 processes which cause the changes in the pore structure. A higher value of n results in higher
709 permeability change with small porosity changes. In the past, a number of experimental
710 studies have reported a range of values for exponent n, corresponding to the dissolution

711 pattern developed in different types of carbonate rocks (e.g., Menke et.al., 2015; Luquot and
712 Gouze, 2009; Luquot et.al., 2014). For example, for a uniformly dissolving Ketton carbonate,
713 Menke et.al. (2015) obtained a value of 5.16 while Luquot and co-workers (2009, 2014)
714 found values of 0.29 and 0.32 corresponding to the development of homogeneous dissolution
715 pattern in Oolitic Limestone. To calculate the exponent, we used half sample length-based
716 porosity and permeability values instead of cropped sample length. This is because, for curve
717 fitting, we had multiple data points from the half sample length while only two data points
718 from the cropped sample length. We obtained the lowest value of n corresponding to the
719 uniform dissolution patterns in the experiment HCHS (Figure 10). For the variety of
720 wormholes formed in the other three experiments, we noted that the value of exponent n lies
721 between 9 and 11 (Figure 11). Luquot et.al. (2014) also obtained a high value of n = 7.07
722 corresponding to the formation of dominant wormholes. Since the initial porous medium
723 structures for the various experiments presented here was similar (Figure S11), this wide
724 range of n values noted in this study most likely reflects the composition of the injected
725 solution, and therefore Da number. Additionally, for all experiments except LCLS, we
726 observed an alignment in the porosity-permeability trend from half sample length and
727 cropped sample length datasets. In the case of experiment LCLS, porosity-permeability
728 changes in cropped sample length indicate a lower exponent compared to in the half sample
729 length. This is due to the initial heterogeneity of sample K2 along the flow direction as also
730 indicated by the difference in the macroporosity values at t=0 (Figure 3b). It cannot be ruled
731 out completely that subtle differences in the initial pore structure of different samples
732 affected the distinct pore structures that evolved during the dissolution experiment.
733 Nevertheless, our results strongly suggest that lower dissolution rates at the sample inlet
734 (experiment LCLS) favor the rapid formation of localized channels compared to solutions
735 with a higher reactivity (experiment NCLS). It can therefore be concluded that adjusting the

chemistry of the injecting fluid creates an interplay between reaction and transport time scales that guide a dissolving porous medium to evolve into different pore structure. This suggests that precaution should be taken in the generalization of a single porosity-permeability model for a range of reservoirs containing formation water of different salinities. Potentially, the impact of Ca^{2+} concentration and salinity can be implemented in the derivation of porosity-permeability models to improve their predictability.

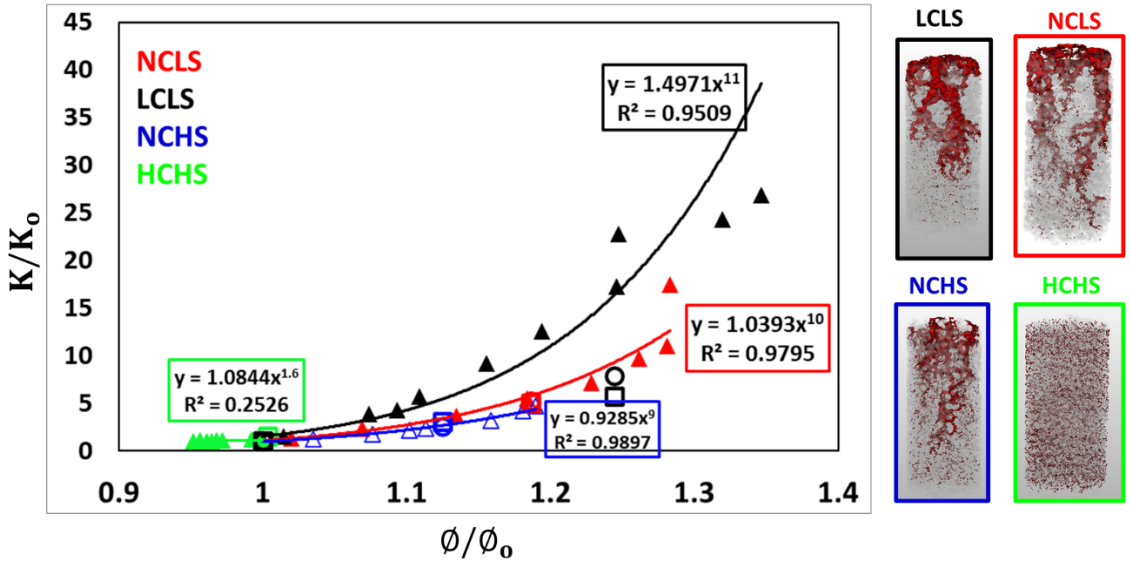

Figure 11: Permeability-porosity relationships for the four experiments. Circle and triangle markers show PNM results for pore network extracted from cropped sample length XMT images and half sample length XMT images, respectively. Square markers show DNS results for the cropped sample length XMT images. Note that the porosity-permeability relationship is obtained by fitting a power-law curve in the PNM based permeabilities of half sample length datasets.

Conclusions

In this study, we employed time-lapse imaging to explore the dissolution of Ketton limestone across four samples under uniform flow conditions but varying reactive conditions, imposed by the composition of injected brine. The imaging highlighted the different stages in the

753 evolution of dissolution patterns, governed by the Da number—subsequently influenced by
754 salt concentration. XMT scans at sequential time steps showedthe constant interplay between
755 changing porosity and permeability of the samples and the evolution of flow patterns and
756 average reaction rates.

757 Our observations highlighted the profound influence of brine composition on alterations in
758 porosity and permeability. The concentration of calcium ions and sodium chloride in the
759 injecting solution emerged as determinants of the calcite dissolution rate, both displaying
760 substantial inhibitory effects. Solutions with minimal salinity and no calcium ions resulted in
761 the most effective calcite dissolution rate, with predominant dissolution near the sample inlet
762 and relatively less along the flow path, creating wormholes with vertically diverse radius
763 profiles. In contrast, solutions with low calcium concentration led to the formation of
764 selective dissolution paths, yielding more uniformly structured wormholes with extensive
765 ramifications. High salt and calcium concentrations significantly decreased dissolution rates,
766 with minimal and uniformly distributed dissolution mainly within the micropore space.

767 In essence, elevated levels of salt and Ca^{2+} ions induced a reaction-limited dissolution regime,
768 maintaining the solution's corrosive properties over extensive penetration depths, resulting in
769 homogeneous dissolution. Conversely, reducing salt and Ca^{2+} concentrations shifted the
770 system towards a transport-dominated dissolution regime, leading to non-uniform dissolution,
771 as the formation of wormholes became evident due to the positive feedback between
772 increased permeability and heightened mass transfer rates (Golfier et.al., 2002).

773 The obtained range of Kozeny-Carman exponents, reflecting the relationship between rock
774 permeability and porosity evolution, was broad, attributed to the variability in the
775 corrosiveness of the injected solutions. To summarize, diverse combinations of salinity and
776 Ca^{2+} concentrations in the injected solution could alter dissolution from a disseminated and

microporous regime to a wormhole regime, resulting in variations in the porosity-permeability relationship. It is important to acknowledge the limitations in this study, such as the absence of lab measurements of porosity and permeability data, leading to uncertainties in quantifying initial pore structures. Addressing these constraints through extended experimental or modelling methodologies will pave the way for enhanced insights in this research direction.

Declaration of competing interest

The authors declare that they have no known competing financial interests or personal relationships that could have appeared to influence the work reported in this paper.

Acknowledgements

The research work of P.A., M.W. and A.R is part of the Industrial Partnership Programme i32 Computational Sciences for Energy Research that is carried out under an agreement between Shell and the Netherlands Organization for Scientific Research (NWO). M.W. has received funding from the European Research Council (ERC) under the European Union's Horizon 2020 research and innovation programme (grant agreement No. [819588]). The XMT experiments in this work were performed at Ghent University's Centre for X-ray Tomography (UGCT), a Centre of Expertise funded by the Ghent University Special Research Fund (BOF-UGent) under grant BOF.EXP.2017.007. TB, AM and VC received funding from the Research Foundation–Flanders (FWO) under project grant G051418N. TB is a postdoctoral fellow of the Research Foundation-Flanders (FWO) and acknowledges its support under Grant 12X0919N. We also thank two anonymous reviewers for their insightful comments, which greatly improved the work.

SUPPORTING INFORMATION AVAILABLE

Additional details on experiment methods and presented results, tables 1-2 and figures 1-27.

801 **References**

802 Akbar M, Vissapragada B, Alghamdi AH, Allen D, Herron M et al (2000) A snapshot of
803 carbonate reservoir evaluation. Oilfield Rev 12:20–40

804 Agrawal, P., Raoof, A., Iliev, O., Wolthers, M., 2020. Evolution of pore-shape and its impact
805 on pore conductivity during CO2 injection in calcite: Single pore simulations and
806 microfluidic experiments. Adv. Water Resour. 136.

807 Al-Khulaifi, Y., Lin, Q., Blunt, M.J., Bijeljic, B., 2017. Reaction Rates in Chemically
808 Heterogeneous Rock: Coupled Impact of Structure and Flow Properties Studied by X-ray
809 Microtomography. Environ. Sci. Technol. 51, 4108–4116.

810 Anabaraonye, B.U., Crawshaw, J.P., Trusler, J.P.M., 2019. Brine chemistry effects in calcite
811 dissolution kinetics at reservoir conditions. Chem. Geol. 509, 92–102.

812 Aslannejad, H., Fathi, H., Hassanizadeh, S.M., Raoof, A., Tomozeiu, N., 2018. Movement of
813 a liquid droplet within a fibrous layer: Direct pore-scale modeling and experimental
814 observations. Chem. Eng. Sci. 191, 78–86.

815 Bedram, A., Moosavi, A., 2011. Droplet breakup in an asymmetric microfluidic T junction.
816 Eur. Phys. J. E 34.

817 Bernabé, Y., Mok, U., Evans, B., 2003. Permeability-porosity Relationships in Rocks
818 Subjected to Various Evolution Processes. Pure Appl. Geophys. 160, 937–960.

819 Boone, M.A., De Kock, T., Bultreys, T., De Schutter, G., Vontobel, P., Van Hoorebeke, L.,
820 Cnudde, V., 2014. 3D mapping of water in oolithic limestone at atmospheric and vacuum
821 saturation using X-ray micro-CT differential imaging. Mater. Charact. 97, 150–160.

822 Buades, A., Coll, B., & Morel, J. M. (2005). A Review of Image Denoising Algorithms, with

823 a New One. Multiscale Modeling & Simulation, 4(2), 490–530.

824 Buhmann, D., Dreybrodt, W., 1987. Calcite dissolution kinetics in the system H_2O-CO_2-
825 $CaCO_3$ with participation of foreign ions. Chem. Geol. 64, 89–102.

826 Bultreys, T., Boone, M.A., Boone, M.N., De Schryver, T., Masschaele, B., Van Hoorebeke,
827 L., Cnudde, V., 2016. Fast laboratory-based micro-computed tomography for pore-scale
828 research: Illustrative experiments and perspectives on the future. Adv. Water Resour. 95,
829 341–351.

830 Daccord, G., Lenormand, R., Liétard, O., 1993. Chemical dissolution of a porous medium by
831 a reactive fluid-I. Model for the "wormholing" phenomenon. Chem. Eng. Sci. 48, 169–178.

832 Elkhoury, J.E., Ameli, P., Detwiler, R.L., 2013. Dissolution and deformation in fractured
833 carbonates caused by flow of CO2-rich brine under reservoir conditions. Int. J. Greenh. Gas
834 Control 16, S203–S215.

835 Esteves, B.F., Lage, P.L.C., Couto, P., Kovscek, A.R., 2020. Pore-network modeling of
836 single-phase reactive transport and dissolution pattern evaluation. Adv. Water Resour. 145,
837 103741.

838 Felmy, A.R., Weare, J.H., 1986. The prediction of borate mineral equilibria in natural
839 waters : Application to Searles Lake , California 50, 2771–2783.

840 Finneran, D.W., Morse, J.W., 2009. Calcite dissolution kinetics in saline waters. Chem. Geol.
841 268, 137–146.

842 Fredd, C.N., Fogler, H.S., 1998. Influence of Transport and Reaction on Wormhole
843 Formation in Porous Media. SPE J. 44, 1933–1949.

844 Garcia-Rios, M., Luquot, L., Soler, J.M., Cama, J., 2015. Influence of the flow rate on

845 dissolution and precipitation features during percolation of CO_2-rich sulfate solutions through
846 fractured limestone samples. Chem. Geol. 414, 95–108.

847 Gledhill, D.K., Morse, J.W., 2006. Calcite dissolution kinetics in Na-Ca-Mg-Cl brines.
848 Geochim. Cosmochim. Acta 70, 5802–5813.

849 Golfier, F., Zarcone, C., Bazin, B., Lenormand, R., Lasseux, D., Quintard, M., 2002. On the
850 ability of a Darcy-scale model to capture wormhole formation during the dissolution of a
851 porous medium. J. Fluid Mech. 457, 213–254.

852 Gray, F., Anabaraonye, B., Shah, S., Boek, E., Crawshaw, J., 2018. Chemical mechanisms of
853 dissolution of calcite by HCl in porous media: Simulations and experiment. Adv. Water
854 Resour. 121, 369–387.

855 Gutjahr, A., Dabringhaus, H., Lacmann, R., 1996. Studies of the growth and dissolution
856 kinetics of the CaCo3 polymorphs calcite and aragonite I. Growth and dissolution rates in
857 water. J. Cryst. Growth 158, 296–309.

858 Hanor, J.S., 1994. Origin of saline fluids in sedimentary basins. Geol. Soc. Spec. Publ. 78,
859 151–174.

860 Harvie, C.E., Weare, J.H., 1980. The prediction of mineral solubilities in natural waters: the
861 NaKMgCaClSO4H2O system from zero to high concentration at 25° C. Geochim.
862 Cosmochim. Acta 44, 981–997.

863 Hoefner, M.L., Fogler, H.S., 1988. Pore evolution and channel formation during flow and
864 reaction in porous media. AIChE J. 34, 45–54.

865 Hoefner, M.L., Fogler, H.S., Stenius, P., Sjoblom, J., 1987. Role of Acid Diffusion in Matrix
866 Acidizing of Carbonates. JPT, J. Pet. Technol. 39, 203–208.

867 Luquot, L., Gouze, P., 2009. Experimental determination of porosity and permeability
868 changes induced by injection of CO_2 into carbonate rocks. Chem. Geol. 265, 148–159.

869 Luquot, L., Rodriguez, O., Gouze, P., 2014. Experimental Characterization of Porosity
870 Structure and Transport Property Changes in Limestone Undergoing Different Dissolution
871 Regimes. Transp Porous Med 101, 507–532.

872 Maheshwari, P., Ratnakar, R.R., Kalia, N., Balakotaiah, V., 2013. 3-D simulation and
873 analysis of reactive dissolution and wormhole formation in carbonate rocks. Chem. Eng. Sci.
874 90, 258–274.

875 Meile, C., Tuncay, K., 2006. Scale dependence of reaction rates in porous media. Adv. Water
876 Resour. 29, 62–71.

877 Menke, H.P., Bijeljic, B., Andrew, M.G., Blunt, M.J., 2015. Dynamic three-dimensional
878 pore-scale imaging of reaction in a carbonate at reservoir conditions. Environ. Sci. Technol.
879 49, 4407–4414.

880 Menke, H.P., Bijeljic, B., Blunt, M.J., 2017. Dynamic reservoir-condition microtomography
881 of reactive transport in complex carbonates: Effect of initial pore structure and initial brine
882 pH. Geochim. Cosmochim. Acta 204, 267–285. https://doi.org/10.1016/j.gca.2017.01.053

883 Molins, S., Trebotich, D., Yang, L., Ajo-Franklin, J.B., Ligocki, T.J., Shen, C., Steefel, C.I.,
884 2014. Pore-scale controls on calcite dissolution rates from flow-through laboratory and
885 numerical experiments. Environ. Sci. Technol. 48, 7453–7460.

886 Morse J. W. and Mackenzie F. T. 1990. Geochemistry of Sedimentary Carbonates. Elsevier,
887 Amsterdam, 707 p.

888 Nan, Z., Shi, Z., Yan, B., Guo, R., Hou, W., 2008. A novel morphology of aragonite and an
889 abnormal polymorph transformation from calcite to aragonite with PAM and CTAB as

890 additives. J. Colloid Interface Sci. 317, 77–82. https://doi.org/10.1016/j.jcis.2007.09.015

891 Nogues, J.P., Fitts, J.P., Celia, M.A., Peters, C.A., 2013. Permeability evolution due to
892 dissolution and precipitation of carbonates using reactive transport modeling in pore
893 networks. Water Resour. Res. 49, 6006–6021.

894 Oral, Ç.M., Ercan, B., Kapusuz, D., 2020. Calcium carbonate polymorph dictates in vitro
895 osteoblast proliferation. J. Aust. Ceram. Soc.

896 Panga, M.K.R., Ziauddin, M., Balakotaiah, V., 2005. Two-scale continuum model for
897 simulation of wormholes in carbonate acidization. AIChE J. 51, 3231–3248.

898 Parkhurst, D., Appelo, C., 2013. Description of Input and Examples for PHREEQC Version
899 3—A Computer Program for Speciation, Batch-Reaction, One-Dimensional Transport, and
900 Inverse Geochemical Calculations.

901 Pereira Nunes, J.P., Blunt, M.J., Bijeljic, B., 2016. Pore-scale simulation of carbonate
902 dissolution in micro-CT images. J. Geophys. Res. B Solid Earth 121, 558–576.

903 Pokrovsky, O.S., Golubev, S. V., Schott, J., 2005. Dissolution kinetics of calcite, dolomite
904 and magnesite at 25 °C and 0 to 50 atm pCO_2. Chem. Geol. 217, 239–255.

905 Raeini, A.Q., Bijeljic, B., Blunt, M.J., 2017. Generalized network modeling: Network
906 extraction as a coarse-scale discretization of the void space of porous media. Phys. Rev. E 96,
907 1–17.

908 Raoof, A., Nick, H.M., Wolterbeek, T.K.T., Spiers, C.J., 2012. Pore-scale modeling of
909 reactive transport in wellbore cement under CO2 storage conditions. Int. J. Greenh. Gas
910 Control 11, 67–77.

911 Schlumberger (2019) Technical challenges—carbonate

912 reservoirs. https://www.slb.com/technical-challenges/carbonates.

913 Soulaine, C., Roman, S., Kovscek, A., Tchelepi, H.A., 2017. Mineral dissolution and
914 wormholing from a pore-scale perspective. J. Fluid Mech. 827, 457–483.

915 Sjöberg, E.L., Rickard, D.T., 1985. The effect of added dissolved calcium on calcite
916 dissolution kinetics in aqueous solutions at 25°C. Chem. Geol. 49, 405–413.

917 Studholme, C., Hill, D.L.G., Hawkes, D.J., 1999. An overlap invariant entropy measure of
918 3D medical image alignment. Pattern Recognit. 32, 71–86.

919 Vlassenbroeck, J., Dierick, M., Masschaele, B., Cnudde, V., Van Hoorebeke, L., Jacobs, P.,
920 2007. Software tools for quantification of X-ray microtomography at the UGCT. Nucl.
921 Instruments Methods Phys. Res. Sect. A Accel. Spectrometers, Detect. Assoc. Equip. 580,
922 442–445.

923 Yoo, H., Kim, Y., Jang, H., Lee, J., 2021. Propagation characteristics of optimum wormhole
924 in carbonate matrix acidizing using micro X-ray CT imaging. J. Pet. Sci. Eng. 196, 108010.

925